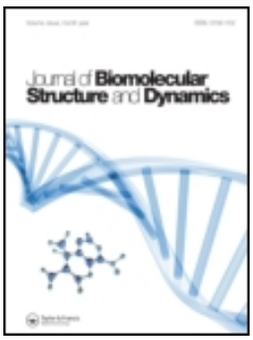

Journal of Biomolecular Structure and Dynamics

ISSN: 0739-1102 (Print) 1538-0254 (Online) Journal homepage: https://www.tandfonline.com/loi/tbsd20

Oxetane Locked Thymidine in the Dickerson-Drew Dodecamer Causes Local Base Pairing Distortions—An NMR Structure and Hydration Study

J. Isaksson , O. Plashkevych , P. I. Pradeepkumar , S. Chatterjee , J. Barman , W. Pathmasiri , P. Shrivastava , C. Petit & J. Chattopadhyaya

To cite this article: J. Isaksson , O. Plashkevych , P. I. Pradeepkumar , S. Chatterjee , J. Barman , W. Pathmasiri , P. Shrivastava , C. Petit & J. Chattopadhyaya (2005) Oxetane Locked Thymidine in the Dickerson-Drew Dodecamer Causes Local Base Pairing Distortions—An NMR Structure and Hydration Study, Journal of Biomolecular Structure and Dynamics, 23:3, 299-330, DOI: 10.1080/07391102.2005.10507067

To link to this article: https://doi.org/10.1080/07391102.2005.10507067

Published online: 15 May 2012.

Submit your article to this journal

Article views: 50

View related articles

Citing articles: 1 View citing articles

Full Terms & Conditions of access and use can be found at
https://www.tandfonline.com/action/journalInformation?journalCode=tbsd20

Journal of Biomolecular Structure & Dynamics, ISSN 0739-1102
Volume 23, Issue Number 3, (2005)
©Adenine Press (2005)

Oxetane Locked Thymidine in the Dickerson-Drew Dodecamer Causes Local Base Pairing Distortions – An NMR Structure and Hydration Study

http://www.jbsdonline.com

J. Isaksson[§]
O. Plashkevych[§]
P. I. Pradeepkumar
S. Chatterjee
J. Barman
W. Pathmasiri
P. Shrivastava
C. Petit
J. Chattopadhyaya[*]

Department of Bioorganic Chemistry
Biomedical Center
Uppsala University
S-751 23 Uppsala, Sweden

[§]Authors have contributed equally in this paper.

Abstract

The introduction of a North-type sugar conformation constrained oxetane T block, 1-(1′,3′-*O*-anhydro-*β*-D-psicofuranosyl) thymine, at the T^7 position of the self-complementary Dickerson-Drew dodecamer, d[(5′-$C^1G^2C^3G^4A^5A^6T^7T^8C^9G^{10}C^{11}G^{12}$-3′)]$_2$, considerably perturbs the conformation of the four central base pairs, reducing the stability of the structure. UV spectroscopy and 1D NMR display a drop in melting temperature of ~10 °C per modification for the T^7 oxetane modified duplex, where the T^7 block has been introduced in both strands, compared to the native Dickerson-Drew dodecamer. The three dimensional structure has been determined by NMR spectroscopy and has subsequently been compared with the results of 2.4 ns MD simulations of the native and the T^7 oxetane modified duplexes. The modified T^7 residue is found to maintain its constrained sugar- and the related glycosyl torsion conformations in the duplex, resulting in staggered and stretched $T^7{\cdot}A^6$ and $A^6{\cdot}T^7$ non-linear base pairs. The stacking is less perturbed, but there is an increased roll between the two central residues compared to the native counterpart, which is compensated by tilts of the neighboring base steps. The one dimensional melting profile of base protons of the T^7 and T^8 residues reveals that the introduction of the North-type sugar constrained thymine destabilizes the core of the modified duplex, promoting melting to start simultaneously from the center as well as from the ends. Temperature dependent hydration studies by NMR demonstrate that the central $T^7{\cdot}A^6/A^6{\cdot}T^7$ base pairs of the T^7 oxetane modified Dickerson-Drew dodecamer have at least one order of magnitude higher water exchange rates (correlated to the opening rate of the base pair) than the corresponding base pairs in the native duplex.

Introduction

Research on the chemistry and interactions of new nucleic acid analogues is a prerequisite for the efficient design of gene directed therapeutic agents like antisense (1-4), aptamers (5-9), and RNA interference (10-13), as well as for the design of sensitive diagnostics arrays (14, 15). A wide array of synthetic building blocks for antisense based therapeutic strategies has already been investigated. These building blocks include different substitutions in the phosphate backbone (16-19), sugar (20-24), or nucleobase (25-33) moieties as well as dynamically constrained bicyclic derivatives of the sugar moiety (34-45). A thorough characterization of different nucleoside analogues can allow us to use novel chemistry to engineer mimics of native nucleic acids with improved properties such as increased specificity and/or binding affinity to the target RNA, increased nuclease stability, rapid delivery into the cell nucleus, and the ability to activate cellular RNA degrading enzymes, like RNase H (46, 47).

Recently, we have developed novel 1′,2′-oxetane locked nucleosides, [1-(1′,3′-*O*-anhydro-*β*-D-psicofuranosyl) nucleosides] (oxetane modified thymidine **T** is shown in Figure 1) which are conformationally constrained to a unique fixed *North-East*

[*]Phone: +46-18 471 45 77
Fax: +46-18 55 44 95
Email: jyoti@boc.uu.se

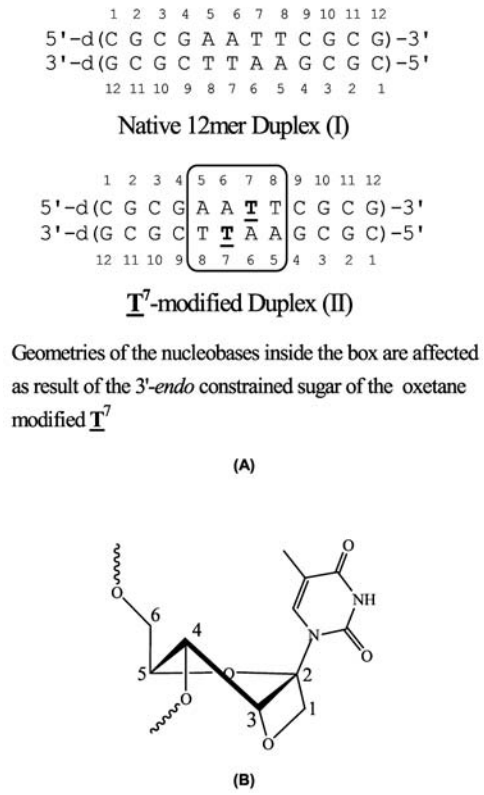

Figure 1: (**A**) Structures of the native Dickerson-Drew (**I**) and $\underline{\mathbf{T}}^7$ modified duplex (**II**). (**B**) Chemical structure of the modified oxetane locked $\underline{\mathrm{T}}$ [1-(1′,3′-*O*-anhydro-β-D-psicofurnosyl) thymine].

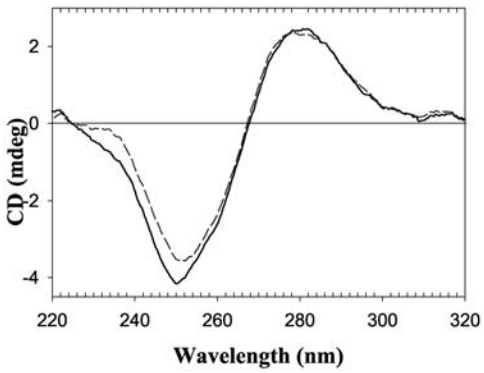

Figure 2: CD Spectra of Native (**I**) (—) and $\underline{\mathbf{T}}^7$ modified (**II**) (– –) Dickerson-Drew dodecamer.

sugar conformation (48-50). Although the T_m of the oxetane-modified antisense-oligo/RNA hybrid drops by ~5-6 °C for incorporation of each oxetane-$\underline{\mathbf{T}}$ modification in to the AON, the mixmer AON/RNA hybrids incorporated with $\underline{\mathbf{T}}$ units were found to be excellent substrates for RNase H promoted cleavage, which is very comparable to that of the native hybrid. However, the incorporation of the oxetane-cytidine ($\underline{\mathbf{C}}$) moiety into the AONs imparts only ~3 °C loss in T_m per oxetane-modification, (51) whereas no loss in T_m is observed for the oxetane-adenosine ($\underline{\mathbf{A}}$) or -guanosine ($\underline{\mathbf{G}}$) modified AONs. The loss of the thermodynamic stability in case of oxetane-$\underline{\mathbf{T}}$ and -$\underline{\mathbf{C}}$ was fully or partly regained by the introduction of the non-toxic DPPZ (dipyridophenazine) group (51) at the 3′ end, which gave also additional stability against exonucleases similar to that of the phosphorothioate AONs (52, 53). The RNase H recruitment capabilities of the oxetane-modified antisense-oligo/RNA hybrid duplexes were found to be very similar to that of the native counterpart. The endonuclease susceptibility of oxetane-modified antisense-oligos was also significantly reduced compared to the native counterpart, and it was proportional to the number of the oxetane modified nucleotides per AON molecule: single modification gave two-fold protection to the cleavage and double and triple modification gave four-fold protection compared to that of the native phosphodiester oligonucleotide (52, 54). The AON constructs with the oxetane-$\underline{\mathbf{C}}$ and 3′-DPPZ were found to be non-toxic in K562 human leukemia cells and have been successfully employed to down-regulate the proto-oncogene c-myb in very efficient manner (51). Based on the amount of AON uptake after delivery, determined by slot blot, it was apparent that the oxetane modified AONs are 5-6 times more efficient antisense agents than those of the corresponding isosequential phosphorothioate analogue (51).

Our recent work on the cronocoulometric measurements (55) have shown that the charge transport through the DNA base stack is perturbed only in the DNA·DNA duplex and not in the DNA·RNA duplex containing modified $\underline{\mathbf{T}}$ in the DNA strand. Although this qualitatively shows that the introduction of a constrained North-type sugar perturbs the helical stacked conformation of a DNA duplex, the study elucidate neither the nature of the conformational disorder created by the constrained conformation of the sugar, nor how far the conformational disorder propagates along the helix from the constrained site.

We here report the NMR constrained structure of the oxetane-$\underline{\mathbf{T}}$ modified Dickerson-Drew dodecamer, 5′-d($C^1G^2C^3G^4A^5A^6\underline{\mathbf{T}}^7T^8C^9G^{10}C^{11}G^{12}$)$_2$-3′ (Figure 1A) obtained using simulated annealing (SA) and constrained Molecular Dynamics (MD) protocol. We also report a comparison of the NMR structure with the results of the constraints-free 2.4 ns MD simulations of the native (**I**) and oxetane-$\underline{\mathbf{T}}$ (**II**) modified Dickerson-Drew dodecamers.

Results and Discussion

CD and UV Data

The CD spectra of both the native (**I**) and the $\underline{\mathbf{T}}^7$ oxetane modified (**II**) duplexes are typically for B-type DNA duplexes (Figure 2). The negative minimum displays a red shift of ~2 nm and the negative/positive ratio decreases by ~10% for the modified duplex compared with the native duplex. This is consistent with a related observation made for 2′-fluoro-2′-deoxyribofuranosyl thymine (North-type conformation) substitution at residue $\underline{\mathbf{T}}^7$ in the Dickerson-Drew dodecamer where the overall profile of the CD spectra is not significantly changed, even though the T_m is decreased by 5.5 °C per modification (20).

The UV melting experiments performed for the $\underline{\mathbf{T}}^7$ oxetane modified dodecamer (**II**) at various salt concentrations have shown a decrease in the T_m by ~10 °C per modification compared to the native duplex (**I**) (at 100 mM of NaCl, Figure 3 and Table SVII in the ***Supplementary Materials***). This is a significantly larger decrease

compared to the ~6 °C per modification decrease found for the non-self-complementary sequences (48-50). This is most likely because the modified residues in the two strands are located in close cross-strand proximity of each other in the duplex, enabling them to cooperatively open up the core of the duplex.

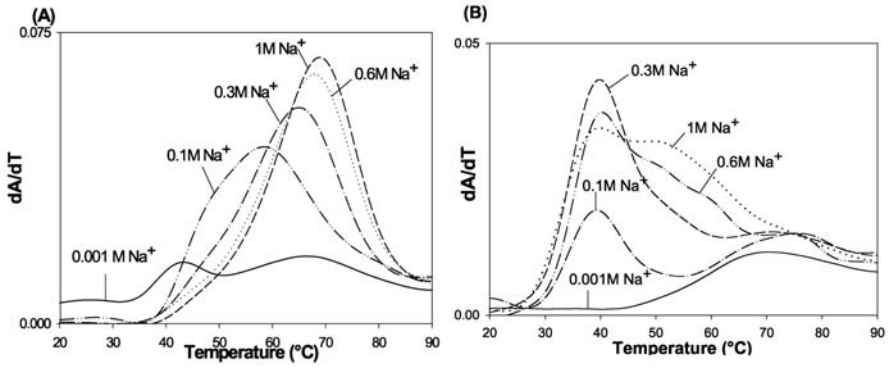

Figure 3: (**A**) Salt concentration dependent (0.001 M to 1.0 M) UV melting curves (first derivative) of (**A**) native Dickerson, and (**B**) **T**-modified dodecamer (10 mM phosphate, 0.1 mM EDTA at pH 7.0 buffer, containing 8 μM in single strand DNA concentration). It is noteworthy that at 0.001 M NaCl concentration, the native dodecamer exists as ca 1:1 mixture of duplex (T_m = 43 °C) and the hairpin (T_m = 66 °C), whereas the **T**-modified dodecamer is exclusively in the hairpin form (T_m = 70 °C). At 0.1 M concentration, we have only duplex for the native (T_m = 43 °C), whereas for the **T**-modified dodecamer, under an identical condition, we have 60/40 mixture of duplex (T_m = 39 °C) and hairpin (T_m = 71 °C).

The native Dickerson-Drew dodecamer (**I**) is known (56) to exist in the form of a duplex or a hairpin structure depending on the salt and oligomer concentrations. At low salt concentration (0.001 M NaCl, 8 μM of DNA), the native dodecamer (**I**) undergo two transitions: (a) a low temperature transition (T_m = 43.2 °C, concentration dependent), corresponding to the melting of the duplex, and (b) a high temperature transition (T_m = 66.2 °C, concentration independent), corresponding to the hairpin to random coil transition (Figure 3A). With increasing salt concentration, the proportion of hairpin structure is gradually decreased and at 0.3 M salt only the duplex to single strand transition (T_m = 64.9 °C) can be observed (Figure 3A). As the salt concentration is further increased, the stability of the duplex form continues to increase and at 1.0 M NaCl concentration the T_m is 68.8 °C.

At low salt concentration (0.001 M NaCl), the melting of the **T** modified dodecamer (**II**) only showed the hairpin to random coil transition (concentration independent) with a T_m of 70.1 °C (Figure 3B in the ***Supplementary Materials***). This is different from the behavior of the native duplex (**I**) that exists in both duplex and hairpin form at this salt concentration (Figure 3 and Table SVII in the ***Supplementary Materials***). The coexistence of the duplex and hairpin forms for the oxetane modified dodecamer is however observed even at 0.1 M NaCl concentration with T_m of 39.3 °C and 71.0 °C, respectively. As the salt concentration is increased from 0.1 to 1.0 M, the hairpin structure of the oxetane modified dodecamer (**II**) almost disappears, but some unknown transitions are observed in the range of 50-60 °C. Surprisingly, increment of the salt concentration from 0.001 to 1.0 M does only cause slight changes of the T_m of the duplex (**II**).

Thus, the oxetane **T** modification in dodecamer (**II**) promotes the formation of the hairpin over the duplex structure at lower salt concentrations as compared to the native dodecamer (**I**), with the hairpin structure of the modified duplex (**II**) being ~4 °C more stable than the native (**I**).

NMR 1D Melting Experiments

The temperature dependent chemical shift changes of the different base protons in the $\mathbf{T}^7$ modified duplex (**II**) directly reflect changes in the micro-environment around them correlated to temperature driven conformational changes. Under NMR conditions, the melting temperature of the H6 of T^7 and 5-Me of T^8 nucleobase protons in the native duplex (**I**) was 74.4 and 73.3 °C, respectively. The corresponding H6 of $\mathbf{T}^7$ and 5-Me of T^8 protons of the modified duplex (**II**) melted at 48.2 and 65.3 °C, respectively (Figure 4). The remarkable difference in melting temperature between the $\mathbf{T}^7$ and T^8 of the modified duplex (**II**) reflects that the modified base pairs are less thermodynamically stable than the neighboring base

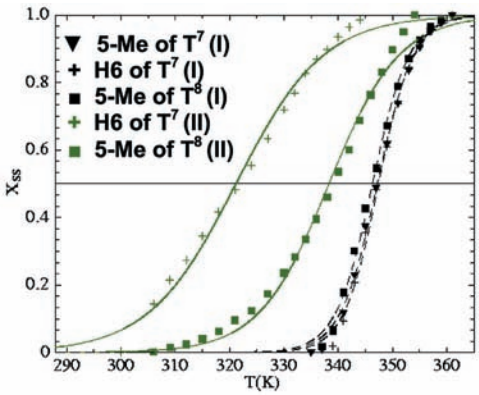

Figure 4: Comparison of the melting of the aromatic- and methyl protons between the native and the $\underline{\mathbf{T}}^7$ modified duplexes. The melting temperature of the native duplex (**I**) was 74.4 and 73.3 °C for H6T^7 and 5-MeT^8, respectively. The same protons of the modified duplex (**II**) melted at 48.2 and 65.3 °C. This supports the observations made for the imino protons, where there appears to be more dynamics at the central A^6-$\underline{\mathbf{T}}^7$ base pairs than in the rest of the duplex.

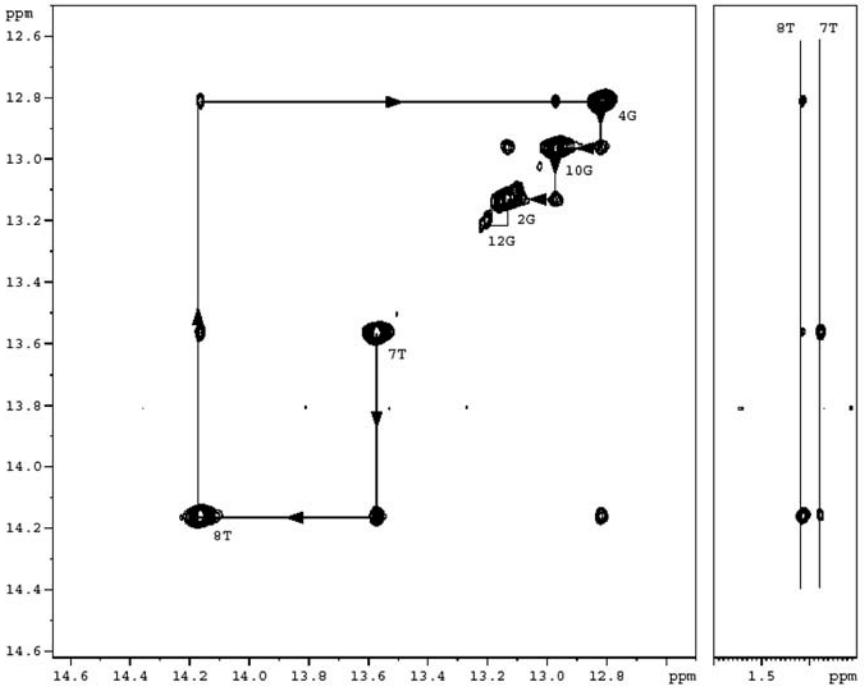

Figure 5: The assignment of the imino protons was straightforward. As for the native Dickerson-dodecamer (**I**), it was possible to trace all imino protons sequentially. An upfield shift of $\underline{\mathbf{T}}^7$ and a downfield shift of T^8 were observed. Further, it was possible to anchor the imino-resonances to the aromatic resonances through the methyl groups of $\underline{\mathbf{T}}^7$ and T^8. Spectrum acquired at 273 K and 300 ms mixing time.

pairs. This increase in dynamics at the center of the duplex (Figure 4) most likely means that the duplex melting goes through a bulge-like structure (or possibly a hairpin structure) under NMR conditions, where the two central base pairs, A^6·$\underline{\mathbf{T}}^7$ and $\underline{\mathbf{T}}^7$·A^6, spend less time in a hydrogen bonded and stacked state even though the stems of the duplex are still held together. Hence, the $\underline{\mathbf{T}}^7$ modified duplex (**II**) melts simultaneously from both the center and from the ends, in contrast to the native duplex (**I**) which only melts from the terminal residues (compare to the imino proton exchange rates shown in Figure 8) (57).

Assignment

The assignment of the exchangeable protons was straightforward. The six expected imino protons were all resonating in the downfield region characteristic for base paired imino protons at 0 °C (21). The imino protons could be traced sequentially, as in the native Dickerson dodecamer: H1G^{12} → H1G^2 → H1G^{10} → H1G^4 → H3T^8 → H3$\underline{\mathbf{T}}^7$ (Figure 5). The connectivity between H1G^4 → 5-MeT^8 → H3T^8 has been used to confirm this assignment. The chemical shifts observed for the imino protons belonging to the ends of the modified duplex are almost identical to the ones of the native, whereas the imino proton of T^8 is shifted downfield by 0.22 ppm and the imino proton of $\underline{\mathbf{T}}^7$ is shifted upfield by 0.25 ppm (Table SI and Figure S2 in the ***Supplementary Materials***). The imino proton of $\underline{\mathbf{T}}^7$ showed typical imino-amino cross-strand cross peaks to A^6, while the amino protons of A^5 could not be detected.

All non-exchangeable protons showed typical B-type DNA pattern for all residues except for the modified residue $\underline{\mathbf{T}}^7$, and were assigned using standard procedures (58-64). All chemical shifts are summarized in Table SI in the ***Supplementary Materials***. The protons of residue $\underline{\mathbf{T}}^7$ were assigned using NOESY, DQF-COSY with- and without ^{31}P decoupling, ^{31}P,^{1}H-correlation with- and without selective ^{1}H pre-saturation, ^{13}C,^{1}H-correlation, and selective and non-selective TOCSY. All experiments were performed at 0 °C and 20 °C. The observed connectivity is shown in Figure 6.

Assignment of $\underline{\mathbf{T}}^7$: The H1′/H1′′ were easily assigned since they are the only resonances belonging to $\underline{\mathbf{T}}^7$ that have strong geminal couplings to each other but no other *J*-couplings. The H4′ proton of the $\underline{\mathbf{T}}^7$ was identified as the most upfield of

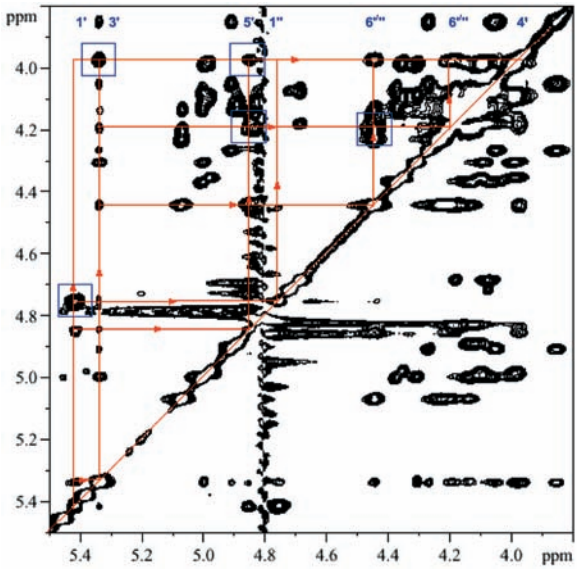

Figure 6: The NOESY cross peaks observed for the modified residue $\underline{\mathbf{T}}^7$ at 293 K and 300 ms mixing time. The peaks that also display DQF-COSY correlations are framed in blue boxes.

the sugar protons because it is the only one that has DQF-COSY cross peaks to two other downfield protons. The proton chemical shift of H4′ of $\underline{\mathbf{T}}^7$ is unexpectedly far upfield, but the 4′-carbon has a chemical shift in the same region as the C4′ atoms of all the native residues. The $^3J_{H4'P}$ coupling is ~7.5 Hz. However, neither H4′, nor H5′ showed any detectable phosphorus coupling. Therefore, the sums of coupling constants were used to determine which resonance belonged to H3′ and H5′, respectively. In this system, the $\Sigma^3J_{H3'} = {}^3J_{H3'H4'}$ and the $\Sigma^3J_{H5'} = {}^3J_{H4'H5'} + {}^3J_{H5'H6'} + {}^3J_{H5'H6''}$. For a North-type conformation, the $\Sigma J_{H5'}$ is never smaller than ~12 Hz regardless of the conformation of the gamma torsion (65). Since the sum of couplings for the first resonance is ~19 Hz and the other is ~5 Hz, the large sum resonance has been assigned to H5′ and the small to H3′. The resonance of H5′ also has one detectable DQF-COSY cross peak to one of the H6's but it is only of moderate strength and very close to the waterline.

Further, the NOESY H6T^8-H3′$\underline{\mathbf{T}}^7$ cross peak is relatively strong, which is commonly seen for the corresponding native H2′ in A-form conformations. All DQF-COSY couplings between the sugar protons of the $\underline{\mathbf{T}}^7$ residue were simulated using NMRSIM and are presented in Figure 7. The assignment was also confirmed by structure refinements completely devoid of constraints involving $\underline{\mathbf{T}}^7$ sugar protons and then retroactively compared to these distance constraints. The same procedure was used for stereospecific assignment of H1′ and H1″.

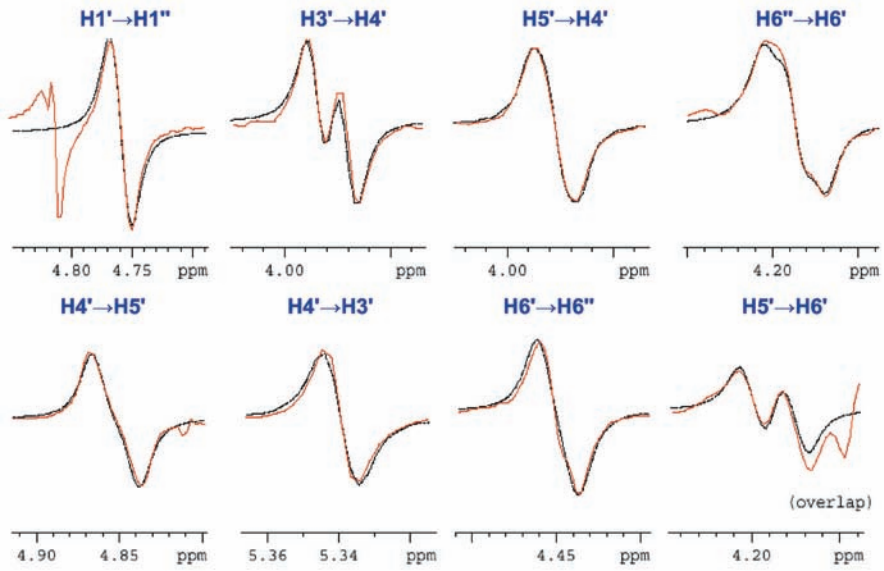

Figure 7: The simulated couplings are compared to cross-sections of the DQF-COSY of duplex (**II**). The simulated couplings were: $^2J_{1'1''} = 9.5$ Hz, $^3J_{3'4'} = 5.0$ Hz, $^3J_{4'5'} = 8.2$ Hz, $^3J_{5'6'} = 8.5$ Hz, $^3J_{5'6''} = 2.5$ Hz, and $^2J_{6'6''} = 14.0$ Hz.

^{31}P resonance assignments were made directly from the H3′ and H4′ of the flanking residues (corresponding to H4′ and H5′, respectively for **T**^{7}). All 11 ^{31}P resonance lines could be found at chemical shifts not shifted more than 0.1 ppm compared to the native duplex (**I**) for all residues except for residue G^{10}, whose phosphorus signal was shifted ~0.2 ppm upfield (Table SI in the ***Supplementary Materials***).

Chemical Shifts

All six imino protons, including the H3 of the **T**^{7} residue, are observable in the characteristic downfield region of the spectra at 0 °C for the modified duplex (**II**), as well as for the native duplex (**I**). These observations show that the modified duplex (**II**) is fully base paired at low temperature.

The chemical shifts of the aromatic protons indicate that the stacking in the oxetane modified duplex is not dramatically different from the stacking in the native counterpart. The H2 proton of A5 shifts 0.34 ppm downfield and the H8 of A6 shifts by 0.18 ppm downfield, indicating that these protons have been repositioned to a less shielded area relative to the shielding cones of the neighboring bases. All other aromatic protons of the central base pairs, *i.e.*, the H8 of A5, the H6 of **T**^{7} and T8 and the H2 of A^{6} all shift less than 0.03 ppm, thus indicating that they are not shifted significantly *relative* to the surrounding nucleobases.

The **T**^{7} imino proton shifts 0.25 ppm upfield which can generally be attributed to weakening of the hydrogen bonding and/or stronger stacking. The T^{8} imino proton shifts 0.22 ppm downfield (Table SI in the ***Supplementary Materials***), which may indicate weaker intra-strand stacking.

Imino Proton Exchange Studies

Temperature-dependency: As the temperature is increased from 0 to 20 °C, the terminal imino proton NMR signal broadens and disappears due to more rapid exchange with the solvent, while the central five imino protons, including that of the oxetane modified **T**^{7}, are clearly observable at 20 °C (Figure 8). As the temperature is further increased, the imino proton of the G^{2}·C^{11} base pair starts to exchange rapidly with water before the more central imino protons in both the native and the modified duplexes due to a weaker stacking stabilization from the terminal base pair. Interestingly, the imino proton of the **T**^{7}·A^{6} base

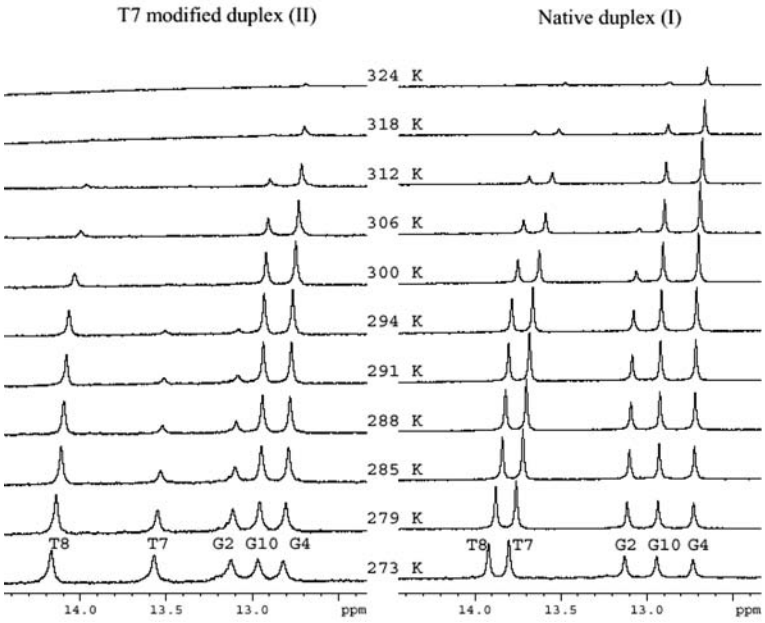

Figure 8: Temperature dependence of the imino protons of the **T**^{7} oxetane modified duplex (**II**) [*left panel*] and of the native duplex (**I**) [*right panel*]. It is evident that the imino proton of the modified **T**^{7} residue exchange rapidly with water at a much lower temperature compared to the native duplex. The imino proton of **T**^{7} broadens out and disappears at 300 K, to be compared to 324 K of the imino proton of the native nucleotide. This behavior is similar to the imino proton of the G^{2} residue of both the native and modified duplexes, which is close to the terminal of the duplexes. Thus, the base pairing dynamics of the two central base pairs in the modified duplex appear to be faster and less stabilized, very similar to the fraying ends of the duplex.

pair in the modified duplex shows a temperature dependence that is very similar to the fraying $G^2 \cdot C^{11}$ base pair (Figure 8). This indicates that the stability of the $\underline{T}^7 \cdot A^6$ base pair is reduced, resulting in increased dynamics of this base pair compared to the native counterpart.

Imino Protons Dynamics: The exchange rates of all non-terminal imino protons ($\underline{T}^7$, T^8, G^4, G^{10}, G^2) have been estimated both by NOESY buildup (**N**) (66) and the NOESY-ROESY approach (**N-R**) (67), as well as from the inversion recovery T_1 and NOESY imino proton line widths (see ***Experimental*** section for details). The calculated rates for both the native (**I**) and the $\underline{T}^7$ modified (**II**) duplexes at 293 K are presented in Table I.

Table I

The imino protons exchange rates [k_{ex}] with the bulk water estimated by the NOESY-ROESY approach, as well as the differences in $T_1[\Delta T_1^{-1}{}_{(II)-(I)}]$ and imino proton line widths [$\Delta\upsilon_{1/2(II)-(I)}$] for the native (**I**) and the $\underline{T}^7$ modified (**II**) duplexes. An error margin of ~20% is estimated for all calculated rates.

				k_{ex} (s^{-1}, 293 K)				
	Base pair	$(R_{1N} + k_{ex})^a$	$(R_{1N} + k_{ex})^a$	**N**[a]	**N-R**[a]	T_1^{-1b}	$\Delta T_1^{-1}{}_{(II)-(I)}{}^b$	$\Delta\upsilon_{1/2(II)-(I)}{}^c$
$\underline{T}^7$ duplex(**II**)	$\underline{T}^7 \cdot A^6$	45	26	5.0	47	11.5	11	15
	$T^8 \cdot A^5$	17	5.6	0.88	0.25	1.2	0.5	4.6
	$C^9 \cdot G^4$	18	4.7	2.3	0.0	0.71	0.0	0.59
	$G^{10} \cdot C^3$	19	5.7	0.52	0.65	0.97	0.1	0.60
	$C^{11} \cdot G^2$	33	15	3.4	7.1	5.3	4.0	5.2
Native duplex (**I**)	$T^7 \cdot A^6$	14	3.1	0.25	0.31	0.68		
	$T^8 \cdot A^5$	15	3.7	0.45	0.61	0.73		
	$C^9 \cdot G^4$	17	4.3	2.3	0.071	0.73		
	$G^{10} \cdot C^3$	17	4.7	0.37	0.42	0.85		
	$C^{11} \cdot G^2$	20	6.5	1.5	2.9	1.3		

[a] See Equations [1-3] in the ***Experimental*** section. R1N is the longitudinal relaxation term. [b] See Equation [4] in the ***Experimental*** section. [c] See Equation [5] in the ***Experimental*** section.

NMR has a very narrow frequency detection range in the millisecond^{-1} scale to study the lifetimes of the exchangeable protons. The increased dynamics of the modified $\underline{T}^7$ base pairs (as well as of the terminal base pairs) imposes a limitation for determination of both too fast ($\underline{T}^7$, G^{12}) and too slow exchange (G^4) rates as both the diagonal and cross peak resonances must be integrated reliably at the studied temperature. Therefore, the rates of exchange have also been estimated from the one dimensional T_1 inversion recovery experiment, and by the direct comparison of the line widths of the imino protons of the $\underline{T}^7$ modified (**II**) and native duplexes (**I**) from the diagonal NOESY resonances (Table I). The native $T^7 \cdot A^6$ base pair has an exchange rate of 0.2-0.3 s^{-1} (corresponding to a base pair lifetime of ~4 s). The T_1 and line widths of the modified $\underline{T}^7 \cdot A^6$ base pair is estimated to have an exchange rate of approximately 10-15 s^{-1} (corresponding to a base pair lifetime of ~0.08 s under the assumption that the base pair opening is rate limiting). The overall destabilization of the duplex is reflected in a small increase in fraying of the G^2 base pair. No significant dynamic deviation from the native duplex (**I**) could however be detected for the $T^8 \cdot A^5$, $C^9 \cdot G^4$, and $G^{10} \cdot C^3$ base pairs.

The conclusive observation is that the opening rate of the modified base pairs is at least one order of magnitude higher than those of the corresponding native base pairs, and that the effect is completely localized as no significant increase in the exchange rate of the neighboring base pairs could be detected. Both the estimated exchange rates (Table I) and the imino proton temperature profile (Figure 8) show that the modified $\underline{T}^7 \cdot A^6$ base pair has increased dynamics and a higher exposure to the bulk solvent compared to the native counterpart, similar to that of the base pairs close to the 5′ and 3′ ends of both the modified (**II**) and the native (**I**) duplexes.

Simulation of the DQF-COSY {^{31}P} coupling constants (Figure 7) and PSEUROT (68) analysis revealed that all native sugar moieties are predominantly in South-type conformation, while the locked **T**^{7} sugar is in North-type conformation (69). The backbone torsion angles (α, β, γ, δ, ε, and ζ) could be partly constrained for most residues using previously published methods (65, 70-74), based on NMR data, using estimated coupling constant co-dependencies and key correlations. The procedures are described in detail in the ***Experimental*** section and all constraints used in the calculation are summarized in Table II.

Table II

Dihedral backbone constraints used (see details in the ***Experimental*** section) in the structure calculations by simulated annealing.

	α	β	γ	δ	ε	ζ	P
C^{1}	-	-	60±40	140±30	180±40	300±40	162±25
G^{2}	300±40	180±40	60±40	140±30	180±40	300±40	150±60
C^{3}	300±40	180±40	60±40	140±30	180±40	300±40	162±25
G^{4}	300±40	180±40	60±40	140±30	180±40	300±40	150±60
A^{5}	300±40	180±40	60±40	140±30	180±40	300±40	162±25
A^{6}	300±40	180±40	60±40	140±30	180±40		162±25
T^{7}		0±140	240±140	80±30	180±40		30±30
T^{8}		180±40	60±40	140±30	180±40	300±40	162±25
C^{9}	300±40	180±40	60±40	140±30	180±40	300±40	162±25
G^{10}	300±40	180±40	60±40	140±30	180±40	300±40	150±60
C^{11}	300±40	180±40	60±40	140±30	180±40	300±40	162±25
G^{12}	300±40	180±40	60±40	140±30	-	-	162±25

Structure Analysis

The NMR constrained structure was solved by X-PLOR (75) using CHARMM22 [MacKerell, Jr. *et al*. (76)] force field and a total of 149 intra-residue, 82 inter-residue and two inter-strand distance constraints, and 64 dihedral constraints per strand. A simulated annealing (SA) protocol in conjunction with full relaxation matrix approach (77, 78) to compensate for spin-diffusion (see ***Experimental*** section for calculation details) was used for the structure determination. Upper bounds of at least 0.5 Å were added to all distance constraints, and structures that did not violate any of the distance boundaries by more than 0.5 Å and no dihedral boundaries by more than 5° were accepted as final structures.

Although NMR constrained SA protocol should produce an experimentally-based structure ideally independent of the force field employed, the insufficient number of the NMR constraints, particularly for defining orientations of the aromatic nucleobases as well as backbone atoms (specifically due to lack of reliable constraints for zeta and alpha torsions), may lead to some local structural uncertainty in the DNA and/or RNA structure, which allows the nature of the applied force fields and the parameters of simulations to become dominating factor. Here the application of the explicit solvent and ionic environment drastically improves the accuracy of the theoretical simulations. Although both CHARMM [MacKerell, Jr. *et al*. (76)] and AMBER [Cornell *et al*. (79)] force fields can reproduce structure and dynamics of DNA [for discussion see Feig and Pettitt (80) and references therein], there remains to be a number of differences in the structure and dynamics of the duplexes produced under identical simulation conditions (81-92). One can expect fluctuation between A- and B-type like structures during the simulation with the CHARMM force field favoring A-type and rarely reaching canonical B-DNA values, and with AMBER force field better reproducing experimental B-type structures and having whole conformational subspace between A- and B-DNA accessible (80).

We have employed the standard SA protocol using the CHARMM22 force field to sample the available hyperspace of the molecule at an artificial temperature as high

as 2000 K. This crude and resilent treatment required to sample the full hyperspace, and therefore we kept the hydrogen bonding intact by relatively tight distance constraints between the hydrogen bonding atoms *in vacuo*.

In order to overcome the intrinsic limitation of the above SA protocol, we have designed complementing 500ps MD simulation making use of the same NMR constraints as in SA protocol and employing modified version (parm98) of the AMBER [Cornell *et al*. (79)] force field, and *explicit water solvent* in presence of potassium counter-ions using Cheatham-Kollman's protocol (83) to compare the NMR structure of the $\underline{\mathbf{T}}^7$ oxetane modified dodecamer (see ***Experimental*** section for details) under two different simulation conditions. The final structures of these (i) SA simulation using NMR-constrained X-PLOR with CHARMM22 and (ii) the NMR-constrained AMBER simulations are presented in Figures 9A-G.

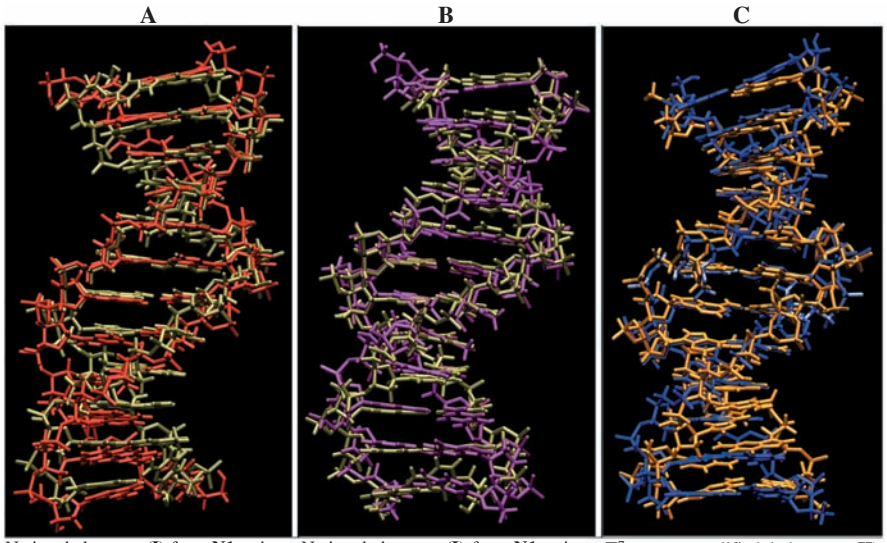

Native dodecamer (**I**) from **N1** trajectory *vs* native by by Denisov *et al*. (21) RMSd = 2.71 Å

Native dodecamer (**I**) from **N1** trajectory *vs* native by Wu *et al*. (93) RMSd = 1.77 Å

$\underline{\mathbf{T}}^7$ oxetane modified dodecamer (**II**) from **D1** trajectory *vs* **D2** trajectory, RMSd = 2.06 Å

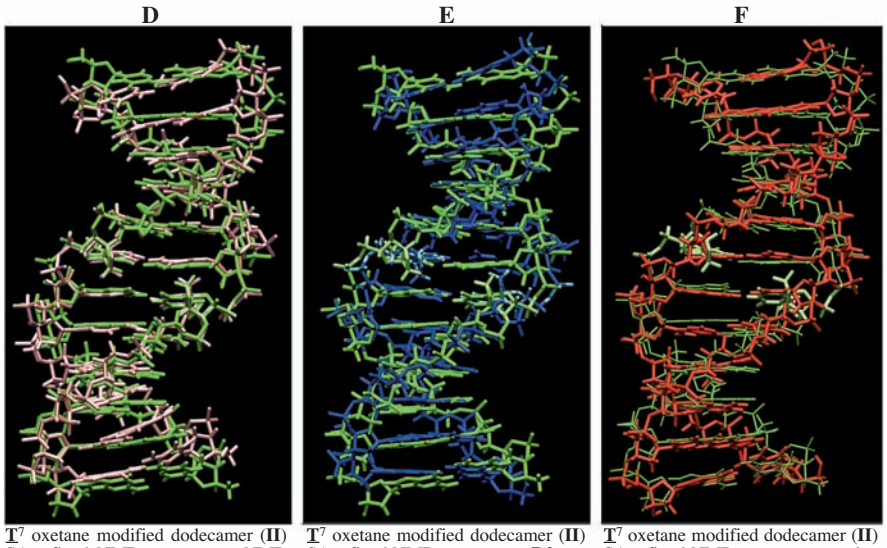

$\underline{\mathbf{T}}^7$ oxetane modified dodecamer (**II**) SA refined NMR structure *vs* NMR constrained AMBER structure. RMSd = 1.71 Å

$\underline{\mathbf{T}}^7$ oxetane modified dodecamer (**II**) SA refined NMR structure *vs* **D2** trajectory. RMSd = 2.08 Å

$\underline{\mathbf{T}}^7$ oxetane modified dodecamer (**II**) SA refined NMR structure *vs* native (**I**) by Denisov *et al*. (21) RMSd =2.29 Å

Figure 9A-F: Pair-wise comparison of the structures obtained for: (i) the native Dickerson-Drew dodecamer (**N1** trajectory) (**panel A**, tan) compared to experimental NMR structures by Denisov *et al*. (21) (**panel A**, red) and Wu *et al*. (93) (**panel B**, purple); (ii) structures of the $\underline{\mathbf{T}}^7$ modified duplex (**II**) obtained during 1.5-2.2 ns of the D1 (**panel C**, orange) and **D2** trajectory (**panel C**, blue); (iii) the NMR constrained simulating annealing CHARMM (green) structure of the oxetane $\underline{\mathbf{T}}^7$ modified duplex (**II**) compared to: (a) the structure from the NMR constrained 0.5 ns AMBER MD simulation (**panel D**, pink); (b) to the average MD structure at the end (1.5-2.2 ns) of the **D2** trajectory (**panel E**, blue); and (c) to the experimental NMR structure of native Dickerson-Drew dodecamer by Denisov *et al*. (21) (**panel F**, red). The backbone RMSd values are shown below each pair of structures.

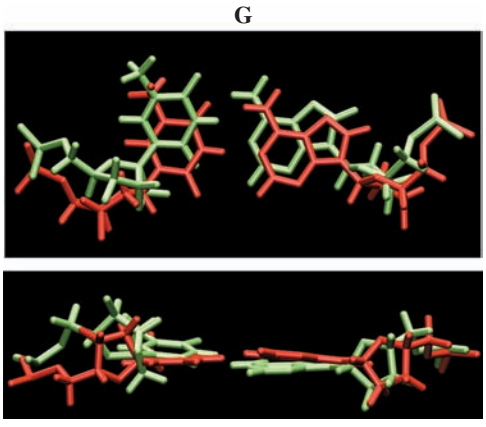

Figure 9G: Superimpositions of the $\underline{\mathbf{T}}^7$·A^6 base pairs of: (i) the NMR constrained simulating annealing structure of duplex (**II**) (green), and (ii) the NMR structure of the native duplex (**I**) Denisov *et al*. (21) (red). The perturbed geometries of the oxetane $\underline{\mathbf{T}}^7$ nucleobases leads to non-linear hydrogen bonds, which affects the stability of the duplex.

To complement these minimized NMR constrained structure with insights into the dynamics of the duplex and to eliminate possible effects of over-constraining, unconstrained MD simulations (2.4 ns at 298K) have been performed for the $\underline{\mathbf{T}}^7$ modified duplex (**II**), starting from canonical B-type DNA (**D1** trajectory) and the final SA NMR constrained structure (**D2** trajectory) (see ***Experimental*** section for details). The molecules were fully solvated in presence of potassium

counter-ions with explicit treatment of the electrostatic interactions using Cheatham-Kollman's protocol (83).

To have intrinsic standard for comparison of the oxetane modified DNA duplex with the native counterpart d(CGCGAATTCGCG)$_2$ (**I**), we have also performed MD simulation of the native Dickerson-Drew dodecamer (**N1** trajectory) which produced results consistent with reported (82-92) MD simulations beyond nanosecond range with full-scale solvation and explicit treatment of electrostatic interaction and employing different force fields. This was also compared with the NMR resolved molecular structure of native Dickerson-Drew dodecamer by Denisov *et al*. (21) and by Wu *et al*. (93) The datasets were sampled every 0.2 ps and the collected trajectories were subjected to both RMSd and energy analysis. The *R*- and *Q*-factors (Table IV and Figure S4 in the ***Supplementary Materials***) of both the native (**I**) and modified (**II**) duplexes from both the SA and MD calculations were extracted from the back-calculated NOE intensities using the CORMA/MARDIGRAS (77, 78) algorithm.

Pair-wise comparison of the structures obtained is presented in Figures 9A-F and 9G for (i) the native Dickerson-Drew dodecamer (**N1** trajectory) (panel A, tan) compared to experimental NMR structures by Denisov *et al*. (21) (panel A, red) and Wu *et al*. (93) (panel B, purple); (ii) structures of the $\underline{\mathbf{T}}^7$ modified duplex (**II**) obtained during 1.5-2.2 ns of the D1 (panel C, orange) and **D2** trajectory (panel C, blue); and (iii) the NMR constrained simulating annealing CHARMM (green) structure of the oxetane $\underline{\mathbf{T}}^7$ modified duplex (**II**) compared to (a) the structure from the NMR constrained 0.5 ns AMBER MD simulation (panel D, pink), (b) to the average MD structure at the end (1.5-2.2 ns) of the **D2** trajectory (panel E, blue), and (c) to the experimental NMR structure of native Dickerson-Drew dodecamer by Denisov *et al*. (21) (panel F, red). The sugar-phosphate backbone of both the native (**I**) and the $\underline{\mathbf{T}}^7$ modified (**II**) duplexes are found to reside mainly in typical B-type DNA conformation, *i.e*., α^-, β^t, γ^+, ε^t, and ζ^- with an exception for the parameters related to the $\underline{\mathbf{T}}^7$ residue. The other geometrical parameters of the duplex also show that the incorporation of the modified nucleoside into duplex (**II**) leads to only a few local changes at the site of modification. The sugar of the oxetane modified $\underline{\mathbf{T}}^7$ residue maintains its North-type conformation and A-type χ torsion, while all other residues retain their typical B-type DNA conformations. The backbone torsion angles are locally perturbed at the site of the oxetane $\underline{\mathbf{T}}$ incorporation. The β torsion is displaced from its normally preferred *trans* (*ap*) conformation to +*gauche* (+*sc*), balanced by a shift of the γ torsion from +*gauche* (+*sc*) to *trans* (*ap*). The α, ε, ζ, and χ torsions of the modified $\underline{\mathbf{T}}^7$ residue are also shifted towards values associated with A-type conformation.

The helical parameter changes have also been found to be mainly localized at the four central base pairs of the oxetane modified duplex. The central $\underline{\mathbf{T}}^7{\cdot}A^6$ and $A^6{\cdot}\underline{\mathbf{T}}^7$ base pairs are strongly staggered and stretched, resulting in distorted non-linear hydrogen bonds between the bases involved. Further, there is a distinct roll of the base pair step between the two modified base pairs, $\underline{\mathbf{T}}^7{\cdot}A^6$ and $A^6{\cdot}\underline{\mathbf{T}}^7$ and there is an increased tilt (and slide) of the $A^5{\cdot}T^8/A^6{\cdot}\underline{\mathbf{T}}^7$ and $\underline{\mathbf{T}}^7{\cdot}A^6/T^8{\cdot}A^5$ base pair steps flanking the two modified base pairs. The main effect on the global structure of the oxetane modified duplex (**II**) is 1 to 3 Å widening of the minor groove width. The structural features of the native (**I**) and $\underline{\mathbf{T}}^7$ modified (**II**) duplexes are discussed in further detail in the following sections.

Sugar Pseudorotational Phase Angle: As a direct reflection of the coupling constant analysis of the DQF-COSY data, both the minimized NMR structures (obtained employing the CHARMM (76), as well as the AMBER (79) force fields) and the unconstrained molecular dynamics structures from **D1** and **D2** trajectories show that all native sugars maintain their preferred South conformations, while the locked $\underline{\mathbf{T}}^7$ sugar remains locked in North-type conformation

(Figure 10). Analysis of the phase angle distributions in the MD trajectories shows that the locked $\underline{\mathbf{T}}^7$ sugar has a phase angle in the range of 26 ± 11° (Figure S8 in the ***Supplementary Materials***). Previous studies (35, 40) on locked nucleosides in non-symmetric hetero duplexes has shown that the sugar conformation affects the sugar conformations of one to two residues in the 3′ direction from the site of the modification. The conclusive result of this study is however that the presence of the locked North-type sugar, $\underline{\mathbf{T}}^7$, residue does not change the overall sugar conformation preference of neither the neighboring- nor the base pairing partner residues. The reason for the more pronounced localization of the sugar effect is most likely due to two-fold symmetry at the site of modification in the studied DNA·DNA homo duplex, making it possible for the two strands to adjust without propagation of the perturbation.

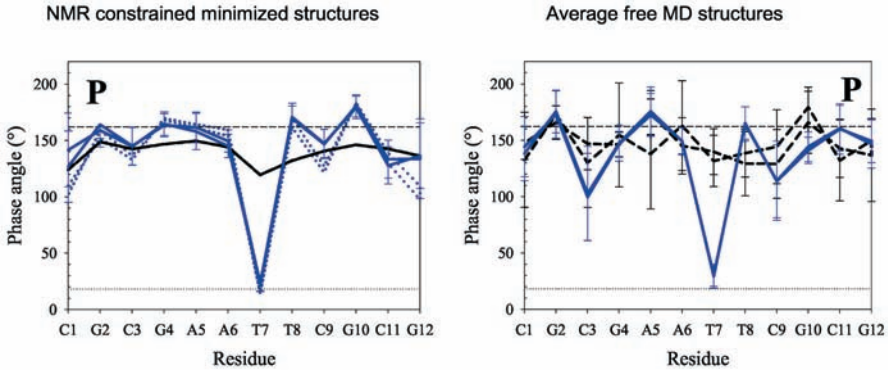

Figure 10: The sugar pseudorotation phase angle, P, of the native (**I**) [- - -] and oxetane $\underline{\mathbf{T}}^7$ modified (**II**) [—] dodecamers. The left panels compare the NMR constrained SA structures of the native (**I**) (21) and $\underline{\mathbf{T}}^7$ oxetane modified (**II**) dodecamers and the right panels show the average values calculated in the 1.5-2.2 ns time interval of the MD trajectories for the unconstrained native (**I**) (**N1** trajectory) and $\underline{\mathbf{T}}^7$ oxetane modified (**II**) (**D2** trajectory) dodecamers The canonical values of B-type (black, short dashed) and A-type (black, dotted) conformations are plotted as horizontal lines for reference.

Sugar-phosphate Backbone Conformation: The *zeta* and *alpha* torsions are in *gauche*$^-$ (*-sc*) conformation in all NMR constrained structures calculated. However, both the *alpha* and *zeta* torsions are configured towards more A-type-like values for the central $\underline{\mathbf{T}}^7$ residue (Figure 11). The same behavior is observed for the *epsilon* torsions – they are all in *trans* (*ap*) conformation, but the central base pairs are shifted towards the ~50° higher value associated with A-type conformation (Figure 11).

In the unconstrained **D1** and **D2** MD trajectories of the $\underline{\mathbf{T}}^7$ oxetane modified DNA, all *epsilon*/*zeta* torsions are in *trans*/*gauche*$^-$ (*ap*/*-sc*) conformation throughout the simulations, except for G^4 and G^{10} whose *epsilon* and *zeta* torsions reside in *gauche*$^-$ (*-sc*) and *trans* (*ap*) conformations, respectively. All phosphates are in BI conformation except the A^5 and C^9 phosphates in the native and the G^4 and G^{10} phosphates in the oxetane modified duplexes, which are predominantly in BII conformation. This observation is statistically stable throughout the 1.5-2.2 ns interval of the simulations, even though these backbone torsions demonstrate the most significant flexibility during the MD simulations.

It should be noted that the presence of BII conformations does not find any support in the NMR observations. No significant $^4J_{H2'P}$ NMR correlation has been observed in the ^{1}H-^{31}P correlation spectra for any native residue, which would have been expected if the *epsilon* torsion had been in *gauche*$^-$ (*-sc*) conformation (71). The presence of any *trans* (*ap*) conformations of either the *zeta* or *alpha* torsions would result in a downfield shift of the phosphorous resonance. A 0.2 ppm downfield shift of the G^{10} phosphorous is observed for the modified duplex (**II**), which may indicate some alteration of the backbone conformation at this position, but we still conclude that the BI conformation is dominant for all native residues in the NMR timescale (ms to s), even if the BII conformation may be populated in the MD simulation timeframe (ps to ns).

The *beta* torsions for all but the $\underline{\mathbf{T}}^7$ oxetane modified residue are found to be in typical B-type DNA *trans* (*ap*) conformation and the *gamma* torsions are in *gauche*$^+$ (*+sc*) conformation. The *beta* torsion of $\underline{\mathbf{T}}^7$ is dislocated from the *trans* (*ap*) conformation where it is normally found in B-DNA structures. This is

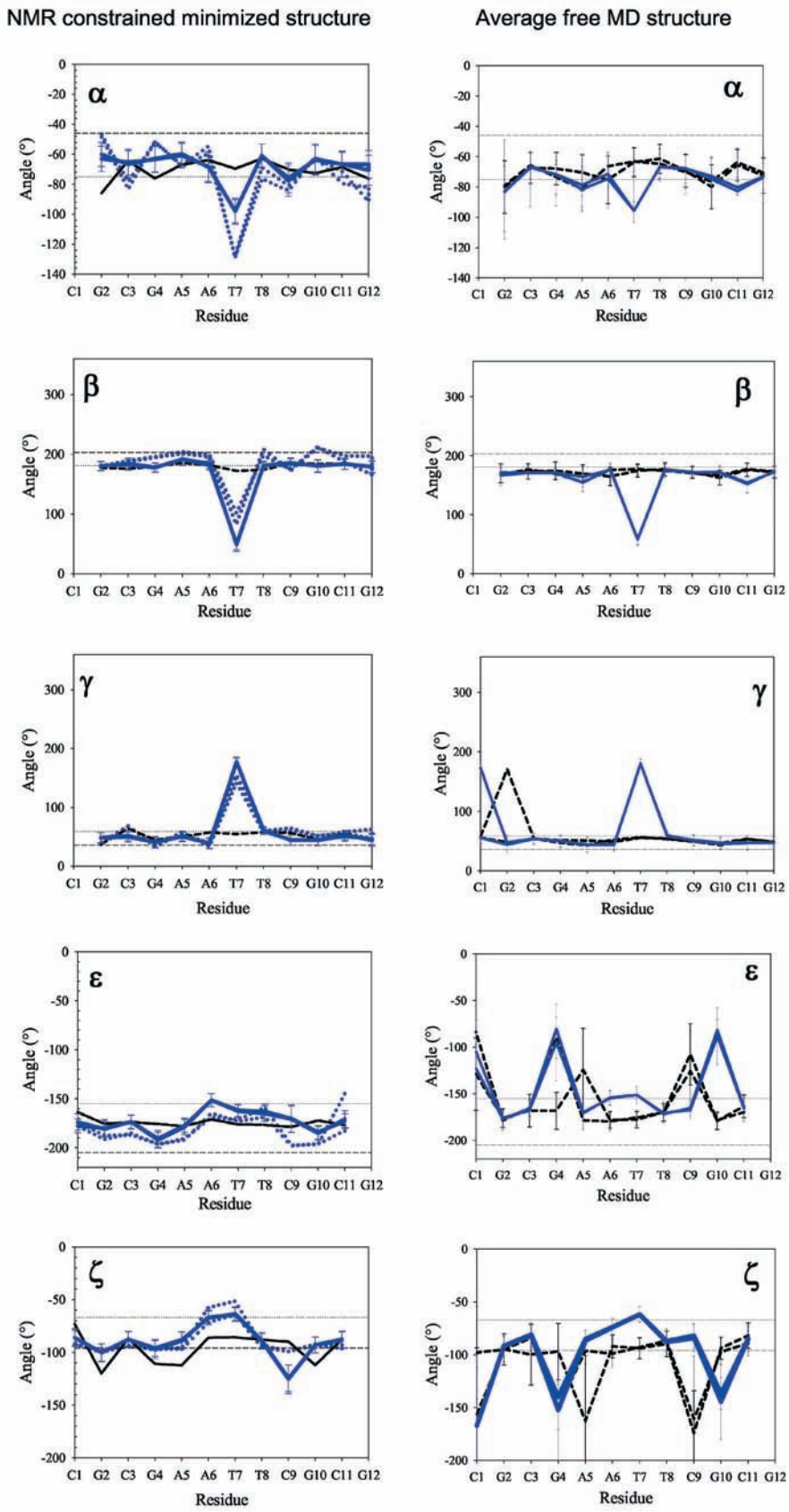

Figure 11: Sugar-backbone torsions of the two strands of the native (**I**) [- - -] and $\underline{\mathbf{T}}^7$ oxetane modified (**II**) [—] dodecamers. The left panels compare the NMR constrained SA structures of the native (**I**) (21) and $\underline{\mathbf{T}}^7$ oxetane modified (**II**) dodecamers and the right panels show the average values calculated in the 1.5-2.2 ns time interval of the MD trajectories for the unconstrained native (**I**) (**N1** trajectory) and $\underline{\mathbf{T}}^7$ oxetane modified (**II**) (**D2** trajectory) dodecamers. The canonical values of B-type (black, short dashed) and A-type (black, dotted) conformations are plotted as horizontal lines for reference.

directly correlated to the absence of the H5′P correlation for the $\underline{\mathbf{T}}^7$ residue together with the presence of a strong coupling between the phosphorus and one of the H6's, which excludes the *trans* (*ap*) domain for the *beta* torsion. The oxetane modification in $\underline{\mathbf{T}}^7$ forces the dislocation of the *beta* torsion from *trans* (*ap*) to *gauche*$^+$ (+*sc*) conformation and a clear preference for *gauche*$^+$ (+*sc*) over *gauche*$^-$ (-*sc*) conformation is observed in both the NMR constrained minimized structure and the MD simulations. The *gamma* torsion for the $\underline{\mathbf{T}}^7$ residue is forced away from the preferred *gauche*$^+$ (+*sc*) conformation, which is populated in both A- and B-type DNA, to a *trans* (*ap*) conformation. This is in agreement with the strong $^3J_{H5'H6'} + {}^3J_{H5'H6''}$ couplings observed for the $\underline{\mathbf{T}}^7$ residue. It is likely that the *beta* and *gamma* torsions of the modified $\underline{\mathbf{T}}^7$ residue are where the impact of the transition from the locked A-type sugar to the B-type sugars of the neighboring residues is absorbed.

Chi Torsion: Since the *chi* torsions are directly correlated to the sugar conformation, the oxetane modification locking the sugar in the $\underline{\mathbf{T}}^7$ residue in North conformation forces the *chi* torsion to be in *trans* (*ap*) conformation, characteristic for A-type DNA, while all other residues are in B-form, with chi torsions in *gauche*$^-$ (-*sc*) conformation (Figure 12). Both the NMR constrained and unconstrained MD structures show these features.

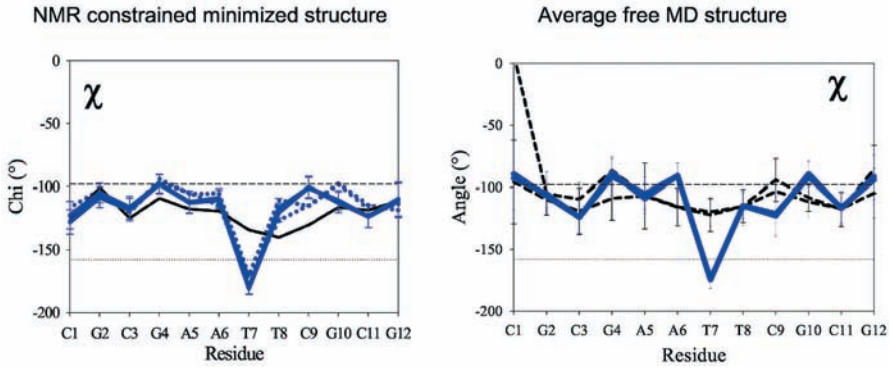

Figure 12: The χ torsion of the native (**I**) [- - -] and oxetane $\underline{\mathbf{T}}^7$ modified (**II**) [—] dodecamers. The left panels compare the NMR constrained SA structures of the native (**I**) (21) and T^7 oxetane modified (**II**) dodecamers and the right panels show the average values calculated in the 1.5-2.2 ns time interval of the MD trajectories for the unconstrained native (**I**) (**N1** trajectory) and $\underline{\mathbf{T}}^7$ oxetane modified (**II**) (**D2** trajectory) dodecamers The canonical values of B-type (black, short dashed) and A-type (black, dotted) conformations are plotted as horizontal lines for reference.

Helical Parameters: The base pair orientation in a duplex is defined by the six complementary base pair parameters, the translational base pair parameters: shear, stretch, and stagger; and the rotational base pair parameters: opening, buckle, and propeller.

The translational parameters of the SA simulated structure (dotted blue lines in Figure 13) show that the central $\underline{\mathbf{T}}^7$·A^6 base pairs of the NMR refined structure (Figure 9) are strongly staggered, stretched and sheared (Figure 13), giving the four bases involved in this double base pair distorted non-linear hydrogen bonds (enlarged in Figure 9G). The shear is displaced by as much as 1 Å in a pattern with alternating positive and negative sign. As the results of unconstrained MD simulations (right panel of Figure 13) does not support the observed amplitude of this distorted zig-zag pattern, we have considered the possibility that this local distortions have resulted from the combination of incomplete set of constraints and the conditions of our SA refinement procedure. We have therefore performed a complementing 0.5 ns MD simulation making use of the same NMR constraints as in SA protocol and employing modified version (parm98) of the AMBER [Cornell *et al*. (79)] force field, solvated in *explicit water* in presence of potassium counter-ions using Cheatham-Kollman's protocol (83) (see ***Experimental*** section for details). The results of this simulation (left panel of Figure 13) produced a lowered amplitude of the shear parameter, closer to that of the unconstrained MD simulations (right panel of Figure 13), modulated the stagger pattern and compensated these changes with an increased opening of the neighboring A^5·T^8 and T^8·A^5 base pairs. This suggests that the SA protocol allows the locked orientations of the two modified base pairs, A^6·$\underline{\mathbf{T}}^7$ and $\underline{\mathbf{T}}^7$·A^6 to shear in

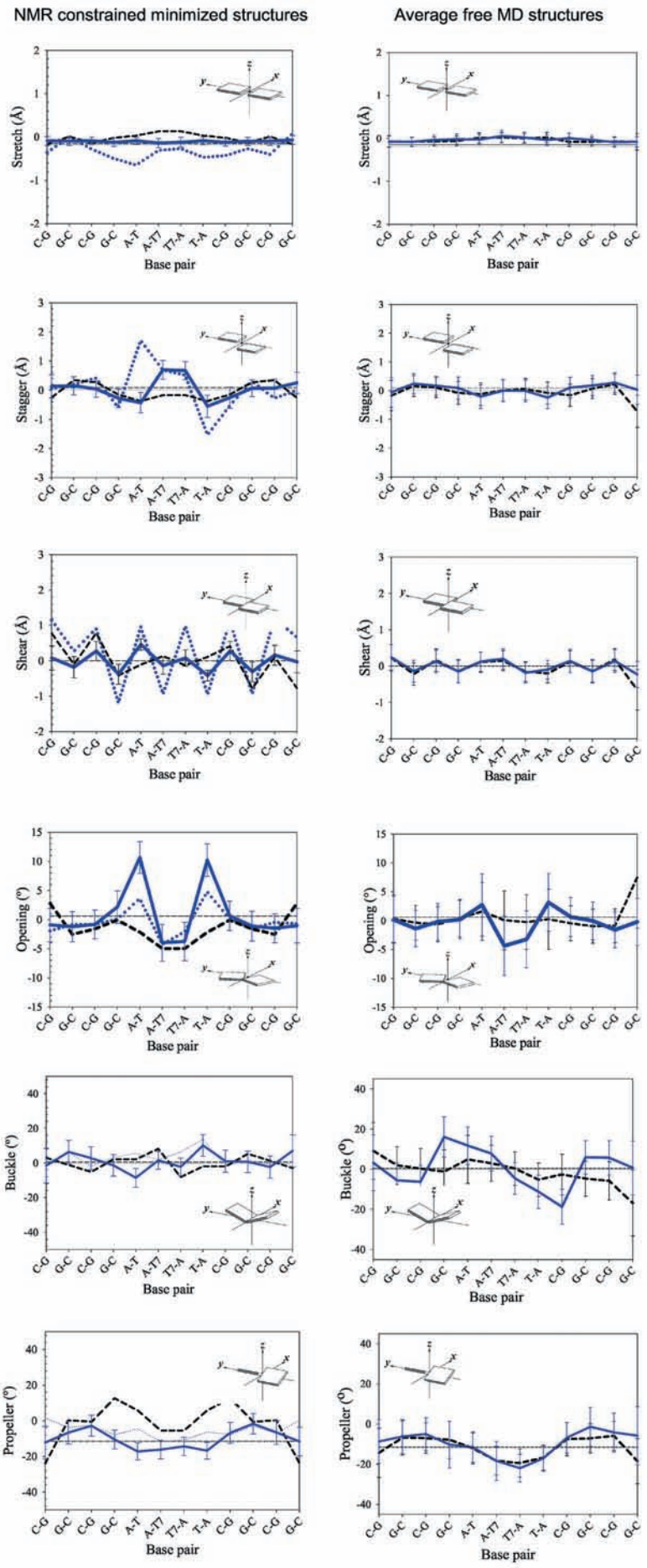

Figure 13: Local base pair parameters of the native (**I**) [- - -] and $\underline{\mathbf{T}}^7$ modified (**II**) [—] (**D2** trajectory) duplexes. The left panels compare the NMR constrained SA structures of the native (**I**) (21) and $\underline{\mathbf{T}}^7$ oxetane modified (**II**) dodecamers and the right panels show the average values calculated in the 1.5-2.2 ns time interval of the MD trajectories for the unconstrained native (**I**) (**N1** trajectory) and $\underline{\mathbf{T}}^7$ oxetane modified (**II**) (**D2** trajectory) dodecamers. The canonical values for B-type (black, short dashed) and A-type (black, dotted) conformation are plotted as horizontal lines for reference.

opposite directions up to a 1.1 Å cutoff where the hydrogen bond constraints distinctly restricts further shearing. This observation is consistent with previously observed alternating shearing pattern of the CGCG ends of the native NMR structure using the same force field, and likely progress the pattern observed for the ends throughout the whole duplex structure.

In contrast, when the more rigorous treatment of the base pairing interactions by the AMBER (parm98) force field is deployed on the native **N1**, and oxetane modified **D1** and **D2** MD unconstrained trajectories, the translational parameters shear, stretch, and stagger are essentially constant for all the base pairs. Thus, the introduction of the oxetane $\underline{\mathbf{T}}^7$ modification changes the average values of the translational base pair parameters negligibly.

No significant changes are observed for the rotational base pair parameters, buckle, and propeller, with the exception of an increased opening of the $\underline{\mathbf{T}}^7$ modified duplex in both the NMR constrained structure and the unconstrained MD structure (Figure 13).

The stacking geometry is described by the six rigid body parameters (shift, slide, rise, tilt, roll, and twist) shown in Figure 14. The base pairs generally remain in stacked conformations for both the NMR constrained structure and the MD average structure. The NMR constrained minimized structure displays some interesting distortions: There is a distinct roll of the base pair step between the two modified base pairs, $\underline{\mathbf{T}}^7{\cdot}\mathrm{A}^6$ and $\underline{\mathbf{T}}^7{\cdot}\mathrm{A}^6$ and there is an increased tilt (and slide) of the base pair steps flanking the two modified base pairs. These distortions of stacking geometry are much less pronounced in the free MD studies.

The additional six rigid body parameters, x-displacement, y-displacement, helical rise, inclination, tip, and helical twist, describe the regularity of the helix (Figure 15). The NMR constrained minimized structure shows symmetric displacement of the helix around the modified residues, while the displacements of the free MD appear less ordered. The helix rise is significantly perturbed between the central four core base pairs and the stems. This may be the reason of the observed unexpected 0.2 ppm downfield shift of the G^{10} phosphate of the modified duplex (**II**) compared with the native (**I**).

Groove Widths: An increase in minor groove width, which is normally associated with A-type conformations, is observed for the central base pairs of both the NMR constrained structure and the free MD structure compared to the native duplex (Figure 16). The minor groove of the free MD structure shows a distinct broadening of ~3 Å at the central residues. The trend is similar in the minimized NMR structure, though the amplitude of the broadening is much smaller, ~1 Å. The major groove width is not remarkably different between the NMR structure and the free MD, even though the NMR structure of the native duplex (**I**) (21) has an unusually wide major groove.

RMSd Analysis

RMSd analysis (Table III) of the average NMR constrained SA structure show that the average $\underline{\mathbf{T}}^7$ modified structure lies within 1.7 Å from the native dodecamer (excluding the terminal base pairs). The four central base pairs are within 0.86 Å of the average free MD structure, showing that the NMR constraints have not imposed excessive amounts of internal strain. Comparison with canonical A- and B-type DNA also shows how the difference between the modified duplex (**II**) and A-type DNA decrease when only the modified core of the duplex is considered (A-DNA: 1.83 Å, B-DNA: 1.57 Å) compared to when the whole duplex is taken into account (A-DNA: 4.23 Å, B-DNA: 2.29 Å). Further RMSd analysis of the MD trajectories is presented in Figure S5 in the ***Supplementary Materials***.

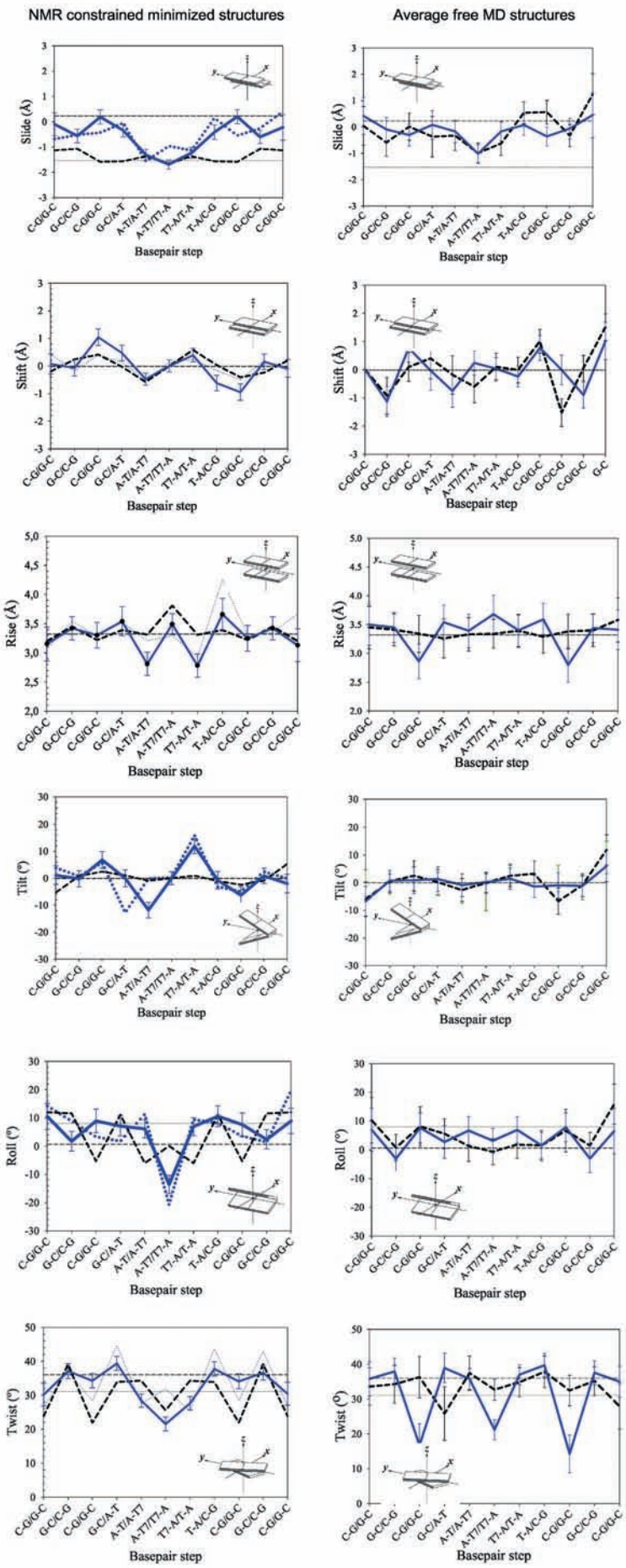

Figure 14: Local base pair step parameters of the native (**I**) [- - -] and $\underline{\mathbf{T}}^7$ modified (**II**) [—] duplexes. The left panels compare the NMR constrained SA structures of the native (**I**) (21) and $\underline{\mathbf{T}}^7$ oxetane modified (**II**) dodecamers and the right panels show the average values calculated in the 1.5-2.2 ns time interval of the MD trajectories for the unconstrained native (**I**) (**N1** trajectory) and $\underline{\mathbf{T}}^7$ oxetane modified (**II**) (**D2** trajectory) dodecamers. The canonical values for B-type (black, short dashed) and A-type (black, dotted) conformation are plotted as horizontal lines for reference.

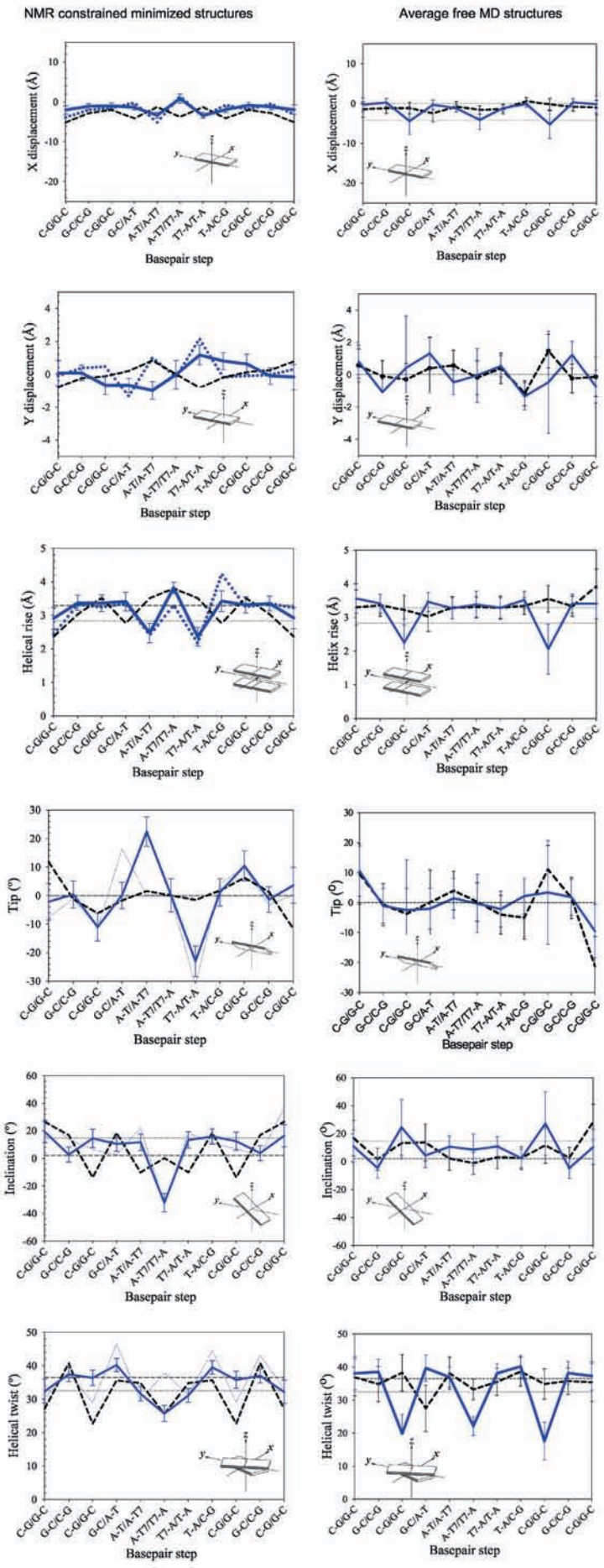

Figure 15: Local base pair helical parameters of the native (**I**) [- - -] and $\underline{\mathbf{T}}^7$ modified (**II**) [—] duplexes. The left panels compare the NMR constrained SA structures of the native (**I**) (21) and $\underline{\mathbf{T}}^7$ oxetane modified (**II**) dodecamers and the right panels show the average values calculated in the 1.5-2.2 ns time interval of the MD trajectories for the unconstrained native (**I**) (**N1** trajectory) and $\underline{\mathbf{T}}^7$ oxetane modified (**II**) (**D2** trajectory) dodecamers. The canonical values for B-type (black, short dashed) and A-type (black, dotted) conformation are plotted as horizontal lines for reference.

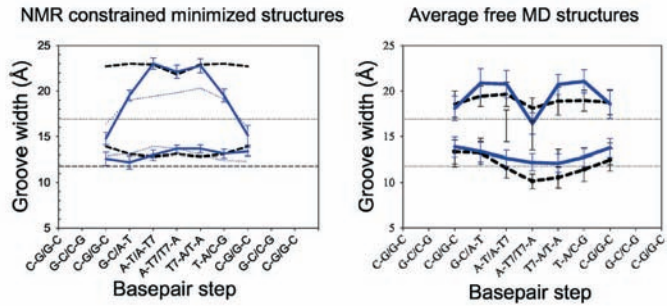

Figure 16: Major- and minor groove widths of the native (**I**) [- - -] and oxetane $\underline{\mathbf{T}}^7$ modified (**II**) [—] dodecamers calculated using 3DNA program package (124). The left panels compare the NMR constrained SA structures of the native (**I**) (21) and $\underline{\mathbf{T}}^7$ oxetane modified (**II**) dodecamers and the right panels show the average values calculated in the 1.5-2.2 ns time interval of the MD trajectories for the unconstrained native (**I**) (**N1** trajectory) and $\underline{\mathbf{T}}^7$ oxetane modified (**II**) (**D2** trajectory) dodecamers. The canonical values for the minor groove width of B-type (black, short dashed) and A-type (black, dotted) conformation are plotted as horizontal lines for reference.

Comparison of the Native Duplex with Canonical B-DNA and NMR Structures: The average RMSds, excluding the two base pairs closest to each of the ends of the duplex (*i.e.*, base pairs $C^1{\cdot}G^{12}$, $G^2{\cdot}C^{11}$, $C^{11}{\cdot}G^2$, and $G^{12}{\cdot}C^1$) of the native dodecamer (**I**) in the **N1** trajectory compared to canonical B-DNA, are 1.88 ± 0.30 Å (1.84 ± 0.30 Å for all residues) at the beginning of the simulation (0.4-0.85 ns) and 1.75 ± 0.36 Å (2.30 ± 0.45 Å), respectively, at the end of the simulation (1.5-2.2 ns). These structures are also close to the native dodecamer (**I**) experimental NMR structure (21) with RMSds of 1.84 ± 0.30 Å for the residues in the middle (2.37 ± 0.40 Å for all residues) at the beginning of the simulation which decreased to 1.72 ± 0.36 Å (2.72 ± 0.40 Å), respectively, at the end. Structures obtained in the **N1** trajectory correlate even better with recently resolved structure (93) obtained on the basis of exceptionally large set of homo- and heteronuclear dipolar couplings and ^{31}P chemical shift anisotropy in bicelle and liquid crystalline medium with RMSds of 1.57 ± 0.25 Å for the residues in the middle (1.84 ± 0.31 Å for all residues) at 0.4-0.85 ns and 1.42 ± 0.29 Å (1.87 ± 0.32 Å) at 1.5-2.2 ns, respectively. The total RMSd fluctuations along the trajectory for the native dodecamer (Figure S5 in the ***Supplementary Materials***) are quite large (up to 1.8 Å between the maximum and minimum RMSd values). Exclusion of the residues at the ends of the strands decreases the magnitude of the RMSd fluctuations to about 1 Å, demonstrating that the residues at the ends of the strands in the native DNA are more flexible than the ones in the middle. The highest amplitude of RMSd fluctuations (up to 2 Å) is, however, observed for the backbone atoms.

Comparison of the Structures from the D1 and D2 Trajectories with the NMR Structure for the T7 Oxetane-modified Duplex: The NMR structure of the oxetane $\underline{\mathbf{T}}$ modified dodecamer refined using SA protocol appeared to be close to that obtained in the subsequent 0.5 ns MD simulations using the same NMR constraints, AMBER force field and explicated solvation yielding average RMSds of 1.07 ± 0.12 Å for the residues in the middle (*i.e.*, excluding base pairs

Table III

The RMSD (Å) of the average NMR constrained SA structure compared to the NMR structure (21) of the native duplex (**I**), the average free MD structure of the modified duplex (**II**), the average free MD structure of the native duplex (**I**), and the canonical forms of B- and A-DNA. The RMSd spread between the average NMR constrained SA structure and the 50 accepted structures is 0.56±0.06 Å for all atoms in the whole duplex.

Modified duplex (**II**) (NMR)	Backbone atoms			Heavy atoms			All atoms		
	All	$G^2{\cdot}C^{11}$	$A^5{\cdot}T^8$	all	$G^2{\cdot}C^{11}$	$A^5{\cdot}T^8$	all	$G^2{\cdot}C^{11}$	$A^5{\cdot}T^8$
Native duplex (**I**) (NMR)	2,09	1,93	1,23	1,77	1,64	1,03	1,83	1,67	1,19
Modified duplex(**II**) (free MD)	2,33	2,10	0,80	2,01	1,83	0,83	2,06	1,85	0,86
Native duplex (**I**) (free MD)	1,85	1,43	1,56	1,58	1,24	1,19	1,72	1,30	1,31
Canonical B-DNA	2,90	2,64	1,60	2,32	2,14	1,38	2,53	2,29	1,57
Canonical A-DNA	5,21	4,81	1,86	4,75	4,17	1,63	4,87	4,23	1,83

$C^{1}{\cdot}G^{12}$, $G^{2}{\cdot}C^{11}$, $C^{11}{\cdot}G^{2}$, and $G^{12}{\cdot}C^{1}$) and average RMSds of 1.38 ± 0.15 Å for all residues. The **D2** trajectory initially showed low average RMSd of 1.17 ± 0.19 Å for the non-terminal residues (1.37 ± 0.17 Å for all residues) that increased after the relaxation of the constraints at the end of the simulation (1.5-2.2 ns) by ~0.6 Å to 1.72 ± 0.16 Å (1.82 ± 0.24 Å), respectively. In the **D1** trajectory the starting B-type DNA structure relaxed rapidly within first 400 ps of the equilibration, and already between 400 and 850 ps of the production run it showed an unexpectedly low average RMSds of 1.50 ± 0.15 Å for the residues in the middle (1.69 ± 0.19 Å for all residues). After approximately 2 ns of the production run (Figure S4 in the ***Supplementary Materials***), the **D1** trajectory converged as its final structures became within 0.5 Å of the final **D2** trajectory's structures, with the average RMSd of 1.74 ± 0.22 Å for the residues in the middle (2.10 ± 0.33 Å for all residues).

The R- and Q-factor Analysis: *R*- and *Q*-factors were calculated using the experimental NOE volumes at 35, 70, and 100 ms mixing times and the theoretical volumes were obtained using 1, 2, and 4 ns as correlation time for every structure and mixing time. The refined NMR structure of the $\underline{\mathbf{T}}^{7}$ oxetane modified DNA is in a good agreement with the NOE experimental data. The *R*-factor of 0.42 and *Q*-factor of 0.21 (Table IV) correspond to a very small difference between the back-calculated theoretical NOE intensities and the measured experimental NOE intensities. For comparison, back-calculated *R*-factors for the canonical B-form and A-form native DNA are 0.6 and 1.1, respectively, compared to the same set of intensities. The R- and Q-factors were also obtained for all structures collected in the **D1** and **D2** trajectories. The results of the *R*-factor analysis for all structures in the **D1** and **D2** trajectories are collected and compared to the results of the NMR refined structures (Table IV).

Table IV
R-factor analysis of the NMR-constrained XPLOR refined structures as well as the **D1** and **D2** trajectories of the $\underline{\mathbf{T}}^{7}$ modified Dickerson-Drew dodecamer, compared to canonical A- and B- DNA structures.

NMR constrained SA structure	R	R^2	R_x	R_x^2	Q	Q^2	Q_x	Q_x^2
	0.42	0.46	0.084	0.11	0.21	0.32	0.042	0.077
D1 trajectory, 1500-2200 ps	0.50	0.55	0.110	0.15	0.25	0.37	0.057	0.107
D2 trajectory, 1500-2200 ps	0.48	0.53	0.101	0.13	0.24	0.36	0.051	0.093
Canonical A-DNA	1.13	1.58	0.20	0.26	0.56	0.83	0.100	0.191
Canonical B-DNA	0.58	0.73	0.12	0.15	0.29	0.47	0.059	0.111

Overall, the *R*- and *Q*-factor fluctuations for both the **D1** and **D2** MD simulations are within 0.03 from the respective average values and in this perspective the *R*-factors do not show any significant development throughout the trajectories (Figure S4 in the ***Supplementary Materials***).

As expected, the *R*- and *Q*-factors are slightly higher for the MD trajectories than the constrained minimized structure from the NMR experiments. The marginal fluctuations of the *R*- and *Q*-factors, together with their low observed average values, show the stability of the simulation in good agreement with the experimental NOE volumes.

Structure Distribution as a Function of Total Energy and RMSd

The MD trajectories of the native duplex (**I**), **N1**, and the trajectories of the modified duplex (**II**), **D1** and **D2**, have been subjected to energetic breakdown analysis.

Total Energy
Native Duplex: The total MM-PBSA energies of the native DNA remains relatively stable during the whole trajectory decreasing by 6 kcal/mol from the start to the end of the simulation (lower panel, Figure S5 in the ***Supplementary Materials***), which is well within the 20 kcal/mol standard deviation observed along the trajectory (Table SIX of the ***Supplementary Materials***).

Table V

Mean internal <E(int)>, van der Waals <E(vdW)>, and electrostatic <E(elec)> energy terms of the total gas-phase <E(gas)> energy, complemented with generalized Born solvation <E(GB)> energy and non-polar contributions to the solvation energy <E(npolar> resulting in the total MM-PBSA energies <E(total)> (gas phase plus solvation) of the duplex and separated strands of the native Dickerson-Drew dodecamer (I) (**N1** trajectory, 1.5-2.2 ns) and of the $\mathbf{T}^7(\mathbf{T}^{19})$ oxetane modified dodecamer (II) (**D1**- and **D2** trajectories, 1.5-2.2 ns). The differences Δ<E(total)> between total energies of the duplex and the two strands of the respective native and oxetane modified DNAs are shown in the last row.

Energy terms, kcal/mol	Native Dickerson-Drew dodecamer						$\mathbf{T}^7(\mathbf{T}^{19})$ oxetane modified dodecamer											
							D1 trajectory						**D2** trajectory					
	1st strand		2nd strand		duplex		1st strand		2nd strand		duplex		1st strand		2nd strand		duplex	
	mean	σ	mean	σ	mean	σ	mean	σ	mean	σ	mean	σ	mean	σ	mean	σ	mean	σ
<E(elec)>	-763.8	17.2	-791.1	14.8	443.4	37.4	-917.7	14.7	-914.6	19.6	154.4	36.8	-924.9	15.4	-929.7	15.9	132.4	47.7
<E(vdW)>	-73.3	5.7	-75.0	5.9	-208.1	10.3	-75.4	5.7	-73.4	5.7	-207.3	9.56	-74.0	5.7	-74.6	5.8	-207.1	9.9
<E(int)>	516.9	14.1	512.9	14.0	1029.8	19.6	555.4	13.8	555.3	13.6	1110.7	19.2	578.2	14.2	580.2	15.3	1158.4	21.1
<E(gas)>	-320.3	19.1	-353.2	16.8	1265.1	37.3	-437.7	18.5	-432.7	21.1	1057.9	40.3	-420.7	18.0	-424.0	18.1	1083.7	47.0
<E(npolar)>	21.6	0.2	21.4	0.2	34.1	0.4	21.2	0.2	21.6	0.2	34.1	0.6	21.4	0.2	21.4	0.2	34.1	0.2
<E(GB)>	-2105.1	15.9	-2080.7	12.5	-6244.5	37.8	-2121.1	12.6	-2124.0	17.6	-6291.4	36.6	-2118.0	14.1	-2113.7	14.0	-6276.9	48.2
<E(total)>	-2403.8	13.3	-2412.4	13.2	-4945.4	19.5	-2537.6	14.3	-2535.1	12.4	-5199.5	19.1	-2517.3	13.3	-2516.4	14.2	-5159.1	20.7
Δ<E(total)>					-129.1	7.1					-126.8	6.5					-125.4	7.0

$\underline{\mathbf{T}}^7$ Oxetane Modified Duplex: In the **D1** trajectory the final structures are about 23 kcal/mol more stable than the initial structures with ~18 kcal/mol energy variation between the structures in 1.5-2.2 ns time interval. The **D2** trajectory was stable in terms of total energy, even though it was converging to structures of 5 kcal/mol higher energy than the initial NMR constrained structure. Since the energy fluctuation in the **D2** trajectory was about 20 kcal/mol in the 1.5-2.2 ns time range and the *R*-factors decreased to a reasonable ~0.4 value, we accepted the final set as converged molecular structures. It should be noted that the standard deviation, σ, has been calculated separately for all energy terms. The standard deviation of the total energy (the energy fluctuation) is about half of the corresponding values for the gas phase and the solvation energies (Table V). This suggests that there is a concerted cancellation of errors in effect, since the total energy is a sum of those two values.

MD: RMSd Versus Total Energy Distributions: There are not any distinct groups of structures indicating multiple state equilibria in the trajectories for either the native duplex (**N1**) or any of the trajectories of the modified duplex (**D1** and **D2**). The structural RMSd between the average structures of the most populated (RMSd 2.0-2.5 Å) and the lowest energy (RMSd 1.5-2.0 Å and 2.5-3.5 Å) groups (Figure S5 in the ***Supplementary Materials***) are below 1.0 Å for both the native duplex (**N1**) trajectory and the trajectories for the modified duplex (**D1** and **D2**). For the **D2** trajectory, the majority of the structures increase their RMSd values by about 0.6 Å upon release of the NMR constraints, although the average distribution of the total energy remains very similar to those of the NMR-constrained structures. The energy-RMSd distributions for all three trajectories showed statistical improvements towards the end of the simulations by getting closer to Gaussian distribution.

Total Gas Phase Energy: The total gas phase energy of the oxetane modified compound is lower compared to that of the native (Table SX and S11 in the ***Supplementary Materials***). This stabilization energy is not homogenously distributed among the different base pairs of the duplex. The two central base pairs containing the oxetane modified **$\underline{\mathbf{T}}$** residues are stabilized by ~85 kcal/mol and their neighboring base pairs are stabilized by ~26 kcal/mol. The rest of the residues have about the same total gas phase energies (observed differences of 0.5-9 kcal/mol are well within the 12 $kcalmol^{-1}$ base $pair^{-1}$ energy fluctuations observed) relative to their native counterpart. Thus, the effect of the introduction of the oxetane modified **$\underline{\mathbf{T}}$** into the DNA duplex is local in terms of energy, propagating directly to one neighboring base pair with only minor influence on the following base pairs. The localized nature of this effect is consistent with the hydration studies, chemical shifts as well as the hydrogen and stacking energy terms discussed in the next paragraphs. It should be noted that the final stabilization of the total gas phase energy originates from the electrostatic energy term, as the internal energy has a destabilizing effect accounting for ~30% reduction of the electrostatic stabilization.

Hydrogen Bonds Energies: The MM-PBSA approach was used to estimate the hydrogen bond energies, using the respective single trajectories to evaluate the difference between the total energy of the duplex and the separated strands of the native and the **$\underline{\mathbf{T}}$** oxetane modified DNAs (Table V). The obtained binding energies are proportional to the strength of the interstrand interactions but mainly reflect the hydrogen bonding and solvation contributions because the stacking energy contributions are canceled out in this approach as the geometries of the separated strands are preserved as in the duplex. The inclusion of the solvation energy is vital, as separated strands are fully solvated which should be reflected in the model. As one can see from Table V, the $\underline{\mathbf{T}}^7$ oxetane modification leads to a destabilization of the modified duplex by 3.2 (**D1** trajectory) and 3.7 (**D2** trajectory) kcal/mol compared to the native counterpart,

which is attributed to the weakening of hydrogen bonds in four central base pairs. It should however be noted that these values are within the standard deviations of about 7 kcal/mol along the trajectories.

Stacking Energies: As base stacking is a complex non-covalent interaction depending on several non-covalent forces (94, 95) – dispersion forces, permanent electrostatic effects of interacting dipoles, and solvation-driven effects – the extraction of the energy attributed to the stacking is not straightforward. We have used the model employed by Hobza *et al*. (96-99), which represents the interaction inside and between the stacked bases including the terms attributed to the hydrogen bonding but neglects all the other interactions in the system. While the interstrand hydrogen bonding is weakened by the introduction of the conformationally locked oxetane modified residues, the stacking still works as a stabilizing force for the oxetane modified DNA. The stabilization energy is dominated by the van der Waals contribution with minor contributions from the electrostatic energy terms, which are most likely underestimated by the theoretical model employed. The

Table VI
Stacking energy (<E(total)>) and its internal (<E(int)>), van der Waals (<E(vdW)>, and electrostatic (<E(elec)>) components calculated for the native and $\underline{\mathbf{T}}^7$oxetane modified dodecamers.

Step	Stacking <E(int)>		Stacking <E(vdW)>		Stacking <E(elec)>		Stacking <E(total)>	
	mean	σ	mean	σ	mean	σ	Mean	σ
Native Dickerson-Drew dodecamers								
$C^1{\cdot}G^{24}/C^{23}{\cdot}G^2$	-0.01	0.09	-24.48	1.02	-1.91	1.50	-26.40	1.86
$G^2{\cdot}C^{23}/G^{22}{\cdot}C^3$	-0.01	0.09	-33.39	1.09	-2.01	1.67	-35.42	1.97
$C^3{\cdot}G^{22}/C^{21}{\cdot}G^4$	-0.02	0.09	-33.02	1.04	0.43	1.68	-32.62	2.01
$G^4{\cdot}C^{21}/T^{20}{\cdot}A^5$	-0.02	0.09	-31.44	1.39	4.85	1.60	-26.61	2.10
$A^5{\cdot}T^{20}/T^{19}{\cdot}A^6$	-0.01	0.07	-30.80	2.10	4.65	1.60	-26.16	2.69
$A^6{\cdot}T^{19}/A^{18}{\cdot}T^7$	-0.01	0.08	-30.60	2.53	3.44	1.83	-27.16	3.04
$T^7{\cdot}A^{18}/A^{17}{\cdot}T^8$	-0.01	0.08	-30.42	2.27	4.63	1.80	-25.80	2.99
$T^8{\cdot}A^{17}/G^{16}{\cdot}C^9$	-0.01	0.08	-30.54	2.00	3.68	1.72	-26.87	2.23
$C^9{\cdot}G^{16}/C^{15}{\cdot}G^{10}$	-0.01	0.09	-31.35	1.62	-0.83	1.90	-32.19	1.92
$G^{10}{\cdot}C^{15}/G^{14}{\cdot}C^{11}$	-0.01	0.09	-30.96	1.15	-3.99	1.62	-34.97	1.85
$C^{11}{\cdot}G^{14}/C^{13}{\cdot}G^{12}$	-0.02	0.09	-21.85	1.36	-4.83	1.74	-26.69	1.77
$\underline{\mathbf{T}}^7$ oxetane modified dodecamer (D1 trajectory)								
$C^1{\cdot}G^{24}/C^{23}{\cdot}G^2$	-0.01	0.08	-24.81	0.93	2.21	1.48	-22.61	1.74
$G^2{\cdot}C^{23}/G^{22}{\cdot}C^3$	-0.02	0.09	-33.45	0.93	3.60	1.38	-29.87	1.62
$C^3{\cdot}G^{22}/C^{21}{\cdot}G^4$	-0.02	0.09	-33.75	0.96	3.91	1.36	-29.86	1.60
$G^4{\cdot}C^{21}/T^{20}{\cdot}A^5$	-0.01	0.07	-32.31	1.31	4.15	1.22	-28.17	1.64
$A^5{\cdot}T^{20}/\underline{\mathbf{T}}^{19}{\cdot}A^6$	0	0.07	-31.28	1.85	4.22	1.51	-27.07	2.30
$A^6{\cdot}\underline{\mathbf{T}}^{19}/A^{18}{\cdot}\underline{\mathbf{T}}^7$	0	0.08	-31.58	1.56	4.30	1.69	-27.28	2.16
$\underline{\mathbf{T}}^7{\cdot}A^{18}/A^{17}{\cdot}T^8$	0	0.08	-31.79	1.40	3.91	1.54	-27.88	2.04
$T^8{\cdot}A^{17}/G^{16}{\cdot}C^9$	-0.02	0.09	-32.11	1.12	5.23	1.30	-26.90	1.52
$C^9{\cdot}G^{16}/C^{15}{\cdot}G^{10}$	-0.02	0.08	-33.36	1.10	5.23	1.63	-28.15	1.77
$G^{10}{\cdot}C^{15}/G^{14}{\cdot}C^{11}$	-0.02	0.09	-33.49	1.07	1.99	1.61	-31.52	1.87
$C^{11}{\cdot}G^{14}/C^{13}{\cdot}G^{12}$	-0.02	0.08	-24.83	0.83	-1.34	1.60	-26.19	1.81
$\underline{\mathbf{T}}^7$ oxetane modified dodecamer (D2 trajectory)								
$C^1{\cdot}G^{24}/C^{23}{\cdot}G^2$	-0.01	0.09	-23.60	1.11	-1.93	1.69	-25.55	2.12
$G^2{\cdot}C^{23}/G^{22}{\cdot}C^3$	-0.02	0.09	-31.93	1.10	-0.70	1.88	-32.65	2.23
$C^3{\cdot}G^{22}/C^{21}{\cdot}G^4$	-0.02	0.09	-32.02	1.20	1.99	1.64	-30.05	2.04
$G^4{\cdot}C^{21}/T^{20}{\cdot}A^5$	-0.01	0.08	-31.35	1.34	3.41	1.45	-27.96	1.86
$A^5{\cdot}T^{20}/\underline{\mathbf{T}}^{19}{\cdot}A^6$	0	0.08	-31.99	1.38	3.84	1.54	-28.14	1.96
$A^6{\cdot}\underline{\mathbf{T}}^{19}/A^{18}{\cdot}\underline{\mathbf{T}}^7$	0	0.08	-32.64	1.55	4.70	1.53	-27.94	2.16
$\underline{\mathbf{T}}^7{\cdot}A^{18}/A^{17}{\cdot}T^8$	0	0.08	-32.03	2.04	4.31	1.57	-27.72	2.65
$T^8{\cdot}A^{17}/G^{16}{\cdot}C^9$	-0.01	0.08	-32.02	1.43	5.10	1.57	-26.92	1.85
$C^9{\cdot}G^{16}/C^{15}{\cdot}G^{10}$	-0.02	0.09	-32.80	1.09	5.34	1.75	-27.48	1.76
$G^{10}{\cdot}C^{15}/G^{14}{\cdot}C^{11}$	-0.02	0.10	-31.57	1.10	2.57	1.53	-29.02	1.74
$C^{11}{\cdot}G^{14}/C^{13}{\cdot}G^{12}$	-0.03	0.09	-22.26	1.21	-0.79	1.38	-23.08	1.84

intra-strand base-base stabilization energy is within 2 kcal/mol of the respective values of the native counterpart (Table VI), including the steps containing the modified residues. The stacking pattern is also similar in the native and the oxetane modified duplexes (Figure S6 in the ***Supplementary Materials***).

The results of the MD simulations, as well as the relatively small differences in the chemical shifts observed for the imino and aromatic protons in the native and oxetane modified dodecamers suggest that while the central four base pairs of the **T**-modified duplex (**II**) are considerably perturbed, the stacking is not significantly altered.

Comparison with Charge Transport Experiment

It has been shown that the long range charge transport through the DNA in cronocoulometric measurements for the $\underline{\mathbf{T}}^7$ oxetane modified DNA occurs at a rate comparable to that of mismatched duplexes (55), which is much lower than the transfer rate for the corresponding native DNA. Our NMR and theoretical results demonstrate that the base pairs containing the oxetane **T** modified residues have a stacked conformation that is similar to the native duplex. Therefore, the stacking geometry of the stacked state alone does not explain the lowered efficiency of the charge transport. The most likely explanation lies in the correlation between the duplex dynamics change upon modification and the time scale for the electrochemical measurements (10^{-2} s) (100). As the transport occurs by a charge hopping mechanism, the modified or mismatched bases have to be fully stacked to modulate the charge transport through the duplex. It has been shown by long range DNA-mediated charge transport and oxidative damage experiments (100, 101) for single base mismatches that the dynamics of the mismatched base pair and its flanking sites, rather than overall helical stability, are the most important determinants of the charge transport efficiency. Correspondingly, the decreased long range charge transfer rate (55) in the oxetane **T** modified duplex (**II**) can be explained by the increased dynamics of the modified and neighboring base pairs. The increased imino proton exchange rates with water as the result of increased opening rate of these bases directly support this hypothesis.

Conclusions

The results of both the NMR experiments and the theoretical MD simulations show that the hydrogen bonds of the $\underline{\mathbf{T}}^7{\cdot}A^6$ and $T^8{\cdot}A^5$ base pairs are significantly perturbed, without significantly affecting the adjoining residues or the rest of the duplex. Thus the duplex maintains overall conformation, closely related to the native counterpart.

Despite the reduction of the T_m, all bases participate in Watson-Crick base pairing. The sugar of the oxetane modified **T** residue is locked into North-type conformation while all other residues retain their typical B-type DNA South sugar conformations. The backbone torsion angles are strongly perturbed at the site of the oxetane **T** incorporation, affecting the quality of the hydrogen bonds in $\underline{\mathbf{T}}^7{\cdot}A^6$ and $T^8{\cdot}A^5$ base pairs. The stacking pattern in the oxetane modified dodecamer is however not found to be significantly different from the native duplex (**I**). The helical parameter changes are found to be mainly localized to the four central base pairs of the oxetane modified duplex. The main effect on the global structure is a 1 to 3 Å widening of the minor groove width at the core of the duplex.

The structural changes are attributed to the restraining effect of the oxetane constrained sugar moiety also constraining the glycosyl torsion (χ) and thereby restricting its ability to find conformations that enables linear base pairing. It does appear that the flexibility of the DNA duplex allows it to absorb most of the anticipated structural impact of the rigid constrained sugar on the rest of the DNA duplex structure. Except for the increase of the minor groove width, the helical

parameters of the non-modified base pairs in duplex (**II**) are not dramatically perturbed compared to the native duplex (**I**).

The temperature dependent 1D NMR melting profile of the imino protons and the hydration studies clearly show that the imino proton of the modified base in the $\underline{\mathbf{T}}^7{\cdot}A^6$ base pair is significantly more exposed to the solvent than the corresponding imino proton in native duplex. Since the imino proton is considered to only exchange with the solvent in the open form of the base pair (66, 67, 102-106) we can conclude that the increased exchange rate of the modified $\underline{\mathbf{T}}^7$ imino proton directly reflects the increased dynamics of this base pair. This behavior is very similar to the fraying effects that are normally observed for the terminal residues of all blunt ended DNA duplexes, making these base pairs contribute less to the overall stability compared to internal base pairs. The 1D melting profile of the non-exchangeable aromatic protons further support this observation since the H6 proton of the modified $\underline{\mathbf{T}}^7$ residue experience destacking at a temperature significantly lower than the melting temperature of the duplex, suggesting that the duplex melts from a bulge formed at the two central base pairs, as well as from the ends.

Thus, the rigid North-type conformation of the $\underline{\mathbf{T}}^7$ residue causes a T_m drop for duplex (**II**) through the destabilization of the core $\underline{\mathbf{T}}^7{\cdot}A^6$ (and $T^8{\cdot}A^5$) base pairs of the duplex leading to a shift in the stacked/destacked equilibrium towards the destacked state, thereby increasing the accessibility of the central base pairs to the bulk water.

The results of the cronocoulometric measurements demonstrate that the long range charge transport through the oxetane modified DNA duplexes occur at a rate comparable to that of mismatched duplexes (55), which is much slower than that of fully base paired duplexes. This is explained by the increased dynamics at the core of the modified duplex, clearly demonstrated by the temperature dependent NMR studies and the hydration experiments.

Our unpublished pK_a determinations of the N3 of thymidine 3′,5′-bis ethyl phosphate (pK_a = 10.12) and (1′,3′-*O*-anhydro-β-D-psicofuranosyl)-thymine 3′,5′-bis ethyl phosphate (pK_a = 9.60) has shown that the electronic equilibrium of the nucleobase is rather strongly affected by the oxetane introduction through the anomeric effect. Decrease in the pK_a difference between the hydrogen bond donor and acceptor ($\Delta pK_a = 0$ for strongest H-bond) is however predicted to strengthen the hydrogen bond rather than weakening it (107, 108). We therefore conclude that the destabilizing effect of the disrupted the linearity of the $A^6{\cdot}\underline{\mathbf{T}}^7$ and $\underline{\mathbf{T}}^7{\cdot}A^6$ hydrogen bonds overweighs the possible stabilizing electrostatic effect of the oxetane modification suggested by the ΔpK_a values of the monomers.

Materials and Methods

Synthesis

The native DNA dodecamer (**I**), 5′-d$(C^1G^2C^3G^4A^5A^6T^7T^8C^9G^{10}C^{11}G^{12})_2$-3′, and the $\underline{\mathbf{T}}$ modified DNA dodecamer (**II**), 5′-d$(C^1G^2C^3G^4A^5A^6\underline{\mathbf{T}}^7T^8C^9G^{10}C^{11}G^{12})_2$-3′, were synthesized and purified using the previously described procedure (48, 50). The optical density was measured at 90 °C to 150 OD_{260} units for the native DNA (**I**) and 80 OD_{260} units for the oxetane $\underline{\mathbf{T}}$ modified DNA (**II**). The oligos were lyophilized twice in D_2O and dissolved in 0.6 ml D_2O (99.96%) or in 9:1 v/v H_2O:D_2O buffer (100 mM NaCl, 10 mM Na_2HPO_4/NaH_2PO_4, 1 mM EDTA, at pH 7.0) for the NMR studies.

UV Measurement

The UV melting profiles have been obtained by scanning A_{260} absorbency *versus* time at a heating rate of 0.5 °C/min in the temperature range from 17 to 90 °C using

a Lamda 40 UV spectrophotometer equipped with Peltier temperature programmer. The T_m was calculated from the maxima of the first derivative of the melting curves. All measurements were carried out in phosphate buffer (100 mM Na_2HPO_4/NaH_2PO_4, 0.1 mM EDTA, pH 7.0), with varying NaCl concentration between 1 mM and 1 M. Before each melting experiment, denaturation, and renaturation of the samples were carried out by heating solutions to 90 °C for 15 min followed by slow cooling to room temperature followed by equilibration at 20 °C overnight. 8 μM of the single strand oligomer was used in all experiments.

CD Measurements

CD spectra were recorded from 320 to 200 nm in 0.2 cm path length cuvettes using JASCO J810-A spectropolarimeter. All the spectra were measured using 4 μM solutions of the DNA duplexes in phosphate buffer [10 mM Na_2HPO_4/NaH_2PO_4 (pH 7.0), 100 mM NaCl, 0.1 mM EDTA] at 5 °C. Each spectrum is an average of five experiments from which the CD value of the buffer was subtracted.

NMR Spectroscopy

All NMR spectra were recorded on BRUKER DRX-500 and DRX-600 spectrometers operating at 500.03 MHz and 600.13 MHz, respectively. For 2D NOESY and ROESY in $H_2O:D_2O$ 9:1, v/v, 4k × 2k × 64 data points were collected in the temperature range from 0° to 35 °C with mixing times of 20, 35, 50, 60, 75, 100, 200, and 300 ms. The water signal was suppressed by the WATERGATE pulse sequence. The water suppression for the NOESY experiments were achieved by the use of two short spinlock pulses, $SL_{\varphi 4}$ and $SL_{\varphi 5}$ (104, 109) using the following parameters: $SL_{\varphi 4}$ and $SL_{\varphi 5}$ are equal to 0.5 μs and 3 μs, respectively, the delay between spinlock pulses is equal to 45 or 150 μs, the carrier was set at the water frequency. For the ROESY experiments, the water suppression was achieved with one short spinlock pulse, $SL_{\varphi 3}$. The used sequence, during the mixing time, of n(π/6) pulses with length 2.5 μs separated by delay, Δ (34.5 μs), corresponds to 6.25 kHz rf field power for pulses. This provides a similar effect as spinlock, $SL_{\varphi 4}$, of the NOESY experiment.

In D_2O, NOESY experiments were run at 0° and 20 °C using the following parameters: mixing times, 35, 70, 100, 150, and 300 ms; 4K complex data points in the f_2 dimension; 1024 or 512 complex data points in the f_1 dimension; relaxation delay of 3 or 5s; sweep width of 10 ppm in both dimensions; 64-128 acquisitions per FID; a Lorenz apodization function for the f_2 dimension; and a shifted sine-bell apodization function for the f_1 dimension. The data was zero-filled in f_1 to give 4K × 4K complex data points. All regions were base corrected separately. The residual water resonance was pre-saturated with very low power during the relaxation delay.

Two-dimensional datasets for DQF-COSY spectra were collected in phase-sensitive mode with time-proportional phase increments, with and without phosphorus decoupling at 0°, 10°, and 20 °C. 4k × 1k × 128 data points were collected in the DQF-COSY experiments. Very weak power pre-saturation was used to suppress the HDO resonance. The data points were resolution-enhanced by a shifted square sine-bell window function in both the f_1 and f_2 dimensions, then Fourier transformed and phase corrected. A relaxation delay of 3 s was used.

TOCSY was run at 0°, 20°, and 30 °C using mixing times of 80 and 120 ms. 4k × 1k × 64-128 data points were collected.

The inverse $^1H^{31}P$-correlation spectra were measured with the delay, τ, in the INEPT step adjusted to give J_{HP} of 5 to 20 Hz, 256 scans and 256 experiments, obtained at 0° to 30 °C.

The inverse $^{1}H^{13}C$-correlation spectrum was acquired on the natural abundance of ^{13}C only, resulting in very poor signal/noise ratio. A total of 4k × 2k × 128 data points were collected and the relaxation delay was 2.5 seconds.

All 2D data was collected on non-spinning samples to avoid t_1 noise.

The transition temperatures (T_m) of duplex to single strand melting for duplex (**1**) and (**2**) were monitored by series of 1D proton spectra covering the temperature range 273 to 354 K in 3 K temperature steps observing the temperature dependent chemical shifts of methyl and aromatic protons for residue $\underline{\mathbf{T}}^7$ and T^8. The 'melting point' was derived by taking the first derivative of the normalized change of chemical shifts. 32k × 128 data points were collected for each spectrum using a sweep width of 10 ppm.

Exchange Rates

The cross peak buildup between the imino protons of G^{12}, G^2, G^{10}, G^4, T^8, and $T^7/\underline{\mathbf{T}}^7$, and the waterline were integrated in NOESY and ROESY experiments in 9:1 H_2O:D_2O using mixing times of 20, 35, 50, and 60 ms. The NOESY cross peaks build-ups were the calculated using the approximation of two isolated protons (66). The diagonal peak intensity is described by Equation [1] and the cross peak between the studied proton and the water line is described by Equation [2].

$$\frac{a_{NN}}{a_{N0}} = \exp[(-R_{1N} + k_{ex})\tau_m] \qquad [1]$$

$$\frac{a_{NW}}{a_{N0}} = \frac{k_{ex}}{R_{1N} + k_{ex} - R_{1W}} \left(\exp(-R_{1N}\tau_m) - \exp[(-R_{1N} + k_{ex})\tau_m]\right) \qquad [2]$$

where, a is the integrated volumes, τ_m is the mixing time, R is the longitudinal relaxation, the index N is used for the studied proton and W for the water proton, and $R_{1W} = 1.03\ s^{-1}$.

The buildup was also treated with the NOESY-ROESY approach (67), which is described by Equation [3], using the same annotations as in Equations [1-2].

$$4\,\frac{a_{NW}^{noe}}{a_{N0}^{noe}} - \frac{a_{NW}^{roe}}{a_{N0}^{roe}} \approx k_{ex}\tau_m \left[3 - \left(\frac{4(R_{NN}^{noe} + R_{WW}^{noe})\tau_m}{2} - \frac{R_{NN}^{roe} + R_{WW}^{roe})\tau_m}{2}\right)\right] \qquad [3]$$

where,

$$R_{NN}^{noe} + R_{WW}^{noe} = 1n\left(\frac{a_{NN}^{noe}}{a_{N0}^{noe}}\right)/\tau_m \text{ and } R_{NN}^{noe} + R_{NN}^{roe} = 1n\left(\frac{a_{WW}^{noe}}{a_{N0}^{roe}}\right)/\tau_m$$

The increase in exchange rate of the modified duplex (**II**) compared to the native duplex (**I**) was also estimated from the inversion recovery T_1 (Equation [4]) (110-115) and the NOESY line widths of the imino protons (Equation [5]) (116).

$$\frac{1}{\tau_{obsd}} = k_{ex} + \frac{1}{T_1^0} \qquad [4]$$

where, $T_1{}^0$ is the longitudinal relaxation rate and τ_{obsd} is the observed life time.

$$\Delta\upsilon_{1/2} = \frac{k_{ev}}{\pi} \qquad [5]$$

where, $\Delta\upsilon_{1/2}$ is the line broadening due to exchange.

Constraints

Sugar and Backbone Constraints:
Sugar Conformation: The sugar conformations of all residues were determined from DQF-COSY experiments with- and without phosphorous decoupling. All

couplings and sums of couplings were estimated from the spectra and then simulated in NMRSIM to generate cross peaks that were identical to the ones from the DQF-COSY {^{31}P}. The sugar motifs of all except the modified residue and the partially overlapped guanosine residues G^{2}, G^{4}, and G^{10}, were estimated to be predominantly (80-100%) in C2′-*endo* conformation using PSEUROT (68) at 20 °C (data not shown). Residues ^{1}C, ^{3}C, ^{5}A, ^{6}A, and ^{8}T-^{9}C, ^{11}C-^{12}G were constrained to P = 162° ± 25°, Φ = 38 ± 4°. The partly overlapped residues were all showing typical B-DNA pattern (73) but since all five couplings could not be individually assessed, some more freedom was allowed. These residues were constrained to P = 150° ± 60°, Φ = 38 ± 4°. The simulated couplings for $J_{3'4'}$ and $J_{4'5'}$ of residue **T**^{7} are very similar to the values found for the monomer (69, 117). Cross-sections of the simulations of the modified residue, **T**^{7}, are presented in Figure 7. The modified **T**^{7} residue was therefore constrained to P = 30° ± 30°, Φ = 38 ± 4° throughout the calculation. No changes in the resulting structure were found in test calculations using no dihedral constraints on the **T**^{7} sugar.

Backbone Constraints: A total of 76 backbone constraints, listed in Table I, were used in the calculation to partly constrained most of the DNA backbone. The constraints were derived using previously described methods (65, 70-74).

Beta (β) and Gamma (γ) Conformation: In a heteronuclear ^{1}H-^{31}P correlation spectrum, the (n)P-(n)H4′ correlation is only detectable when the four bonds in the H4′-C4′-C5′-O5′-P backbone are located in the same plane forming a W-shaped conformation (70, 74). This is possible when the β and γ torsion angles are *trans* and *gauche*$^{+}$ respectively, as in the case of B-DNA. The presence of observable (n)P-(n)H4′ cross peaks (data not shown) for residues G^{2}-A^{6} and T^{8}-G^{12} allowed us to constrain these residues to β^{t} and γ^{+}. The γ torsion in *gauche*$^{+}$ will result in very weak couplings to both the H5's (1.0-2.5 Hz) while both *trans* and *gauche*$^{-}$ will result in a strong (~10 Hz) coupling between the H4′ and one of the H5's (Table SIV in the ***Supplementary Materials***). The modified residue, **T**^{7}, was the only residue with a strong coupling between H5′ and any of its H6's. The β and γ torsions were also confirmed using the linewidths of the NOESY cross peaks of H6/H8 to H4′ (65, 71) for these residues, but no tighter constraints were derived from this. Further, the population of *beta* over time was estimated using the $^{4}J_{C4'P}$ coupling. Close to 100% *trans* conformation was found for residue C^{1}-A^{6} and C^{9}-C^{11} using the $^{\%}\beta^{t} = 100\ (^{3}J_{C4'P} - 0.7)/10.3$ approximation. However, the signal to noise ratio in this experiment was rather poor since the sample only had the natural abundance of ^{13}C and was therefore only used together with the other observations to constrain the backbone of these residues to β^{t} and γ^{+}.

Epsilon (ε) Conformation: If ε is in *gauche*$^{-}$ conformation it should produce a detectable $^{4}J_{H2'P}$ coupling, while if ε is in *trans* conformation no significant $^{4}J_{H2'P}$ will be observable (71). Thus, the absence of cross peaks in ^{1}H-^{31}P correlation spectra allowed us to rule out ε^{-} for all residues, thereby constraining them to the *trans* conformation (BI-type) since *gauche*$^{+}$ appears to be sterically forbidden (95). This could be confirmed by $^{3}J_{C4'P3'}$ ($^{3}J_{C5'P4'}$ for **T**^{7}) values of ~10-12 Hz for all residues except for **T**^{7} and T^{8} who could not be properly assessed in the relatively weak natural abundance ^{13}C^{1}H correlation spectrum (Table SV in the ***Supplementary Materials***).

Alpha (α) and Zeta (ζ) Conformation: For ζ and α we used the qualitative ^{31}P chemical shifts argument (from inverse ^{1}H-^{31}P-correlation spectra at 20 °C) to exclude the *trans* domain (74). A ζ^{-}/α^{-} conformation will have a relatively more upfield chemical shift than both the ζ^{t}/α^{-} and the ζ^{-}/α^{t} conformations. As all our chemical shifts were in the normal range compared to the native duplex (**I**) (21) for all residues, *i.e.*, from -3.7 to -4.1 ppm at 20 °C, we concluded that *gauche-gauche* phosphate ester conformations prevail over the trans conformations (Table SVI in the ***Supplementary Materials***). However, since we are unaware of how the 1′,3′-

O-anhydro-modification affects the ^{31}P chemical shift, we decided not to constrain ζ of A^6 and $\underline{\mathbf{T}}^7$ and α of $\underline{\mathbf{T}}^7$ and T^8.

Chi (χ) Torsion: From the aromatic-H1′ region of NOESY spectra (Figure S1 in the ***Supplementary Materials***) it can be concluded that all nucleobases are in *anti*-conformation. If the conformation of the nucleobases are in *syn*-conformation, the H2 proton of the adenosine residues is further away from the H1′, while the H8 proton is closer to the H1′, thus resulting into considerably stronger intensity of the H8-H1′ cross peak, and the disappearance of the H2-H1′ cross peak. Since neither of these observations can be made for any of the residues, we conclude that all the residues form *anti-anti* Watson-Crick base pairs. This is also supported by the fact that all H6/H8-H2′/′′ distances appear in the expected range for B-type conformation (95) and detectable $H6/H8_n$-$H6/H8_{n+1}$ NOE connectivity for all nucleotide steps.

NOE Constraints: NOE cross peaks from NOESY spectra with mixing times of 35, 70, and 100 ms were integrated using the Aurelia software (118) provided by Bruker. A total of 149 intra-residue, 82 inter-residue, and two inter-strand cross peaks per strand were used in three cycles of X-PLOR/MARDIGRAS refinement. The upper and lower distance boundaries were never allowed to be tighter than 0.5 Å around the distance restraint. The average upper boundary was 0.73 Å from the distance restraint for the MARDIGRAS (77, 78) treated intensities. Ninety-one cross peaks could not be integrated for all mixing times due to spectral overlap, unfavorable dynamics, or water exchange and were instead estimated as strong, medium, or weak and were added in the structure calculation as distance constraints of 1.8-3.5, 2.0-5.0, and 3.0-6.0 Å, respectively. This gives a total average of 27 distance constraints per residue. All inter-residue NOE cross peaks that were used in the calculation are plotted in Figure S3 in the ***Supplementary Materials***.

The NOE constraints derived from very short mixing time (35 ms), where the effects of spin diffusion are close to negligible, were used to generate ten structures using the protocols described above. All volumes of the cross peaks were translated to distances using the two-proton approximation with the H5-H6 cross peaks of the cytidines as reference peaks (2.45 Å). The resulting structures from a simulated annealing run using X-PLOR (75) were then used as a first structural input in the first MARDIGRAS/RANDMARDI (77, 78) cycle. The full relaxation matrix approach was applied using the intensities from three mixing times (35, 70, and 100 ms) and three correlation times for the duplex (1, 2, and 4 ns) to calculate a full set of distance constraints corrected for spin-diffusion effects. The treated NOE constraints were then used to generate the next generation of X-PLOR structures which were subsequently looped back into MARDIGRAS again. After three cycles of MARDIGRAS/XPLOR refinements the final structures were calculated. Generated A- and B-type DNAs were used as starting structures in all X-PLOR structure refinements. Through every cycle, the NOE constraints from MARDIGRAS were merged with the non-integrated peaks.

NMR Structure Refinement Protocol

The charges, bond lengths and angles of the 1′,3′-*O*-anhydro-containing thymidine moiety were optimized at the Hartree-Fock level using 6-31G* basis set. The geometry optimization has been carried out for the anion of the $\underline{\mathbf{T}}$ monomer and the obtained parameters were added to the force field as a new residue type.

The Simulated Annealing (SA) protocol by Omichinski *et al*. (119) was first applied followed by two refinements using the standard refine protocol in X-PLOR 3.1 (75), running the modified CHARMM22 force field parameters suggested by Varani (64).

The SA starts with initial phase comprising 10 ps of dynamics (2 fs steps) at 2000K with the following force constants: NOE, 2 kcal $mol^{-1}Å^{-2}$; dihedral, 10 kcal mol^{-1}

rad^{-2}; bonds, 1000 kcal mol^{-1}Å^{-2}; angles, 200 kcal mol^{-1}rad^{-2}; impropers, 50 kcal mol^{-1}rad^{-2}; and van der Waal, 1 kcal mol^{-1}Å^{-4} (scale factor 1.2). In the next phase the system is cooled from 2000 to 100K in 0.316 ps steps (reducing the temperature by 25 K for each cycle). The NMR-derived dihedrals, 200 kcal mol^{-1}rad^{-2}; bond, 1000 kcal mol^{-1}Å^{-2}; and NCS, 5 kcal mol^{-1}Å^{-2} are kept constant during this phase while the following constants are scaled up for each cycle (*initial-final*): NOE, 2-30 kcal mol^{-1}Å^{-2}; angles, 200-500 kcal mol^{-1}rad^{-2}; and van der Waal, 0.004-4 kcal mol^{-1}Å^{-4} (the radius scale factor for van der Waal is decreased from 0.9 to 0.8 during this phase). Finally, 500 steps of Powell minimization are applied.

The standard refinement protocol was then applied two times in succession with cooling from 1000K to 100K and 500K to 100K, respectively. The NCS was added with the force constant of 10 kcal mol^{-1}Å^{-2} during the second refinement. The number of cooling steps was increased to 10,000 and 20,000, and the number of Powell minimization steps to 1000 and 2000 in the two refinement steps, respectively. The force constants used were: 50 kcal mol^{-1}Å^{-2} for NOE; 200 kcal mol^{-1}rad^{-2} for dihedrals; 1000 kcal mol^{-1}Å^{-2} for bonds; 500 kcal mol^{-1}rad^{-2} for angles; 500 kcal mol^{-1}rad^{-2} for impropers; 0.1-4 kcal mol^{-1}Å^{-4} for van der Waals; and 10 kcal mol^{-1}Å^{-2} for NCS.

The starting structures for the calculations were two stretched out anti-parallel DNA-strands with A- and B-DNA type stems, respectively, and a total of 100 structures were refined each X-PLOR cycle. Because of its restricted nature, the $\underline{\mathbf{T}}^7$ residue and its base pairing partner, A^6, was in North conformation for both starting structures at the start of the calculation.

A 100 ps constrained MD in 293 K was then run using the minimized structure as initial structure using 0.001 ps time steps. All force constants were kept at the same values they had in the final step of the last refinement protocol (see above). The same distance- and backbone constraints were used as in the simulated annealing protocols with the exception that the sugar pucker constraining dihedrals (ν0-ν4) were released to relax any imposed strain in the sugar conformations. Ten structures per ps were stored and averaged in clusters of 5 ps.

Further refinement of the NMR constrained structure of the $\underline{\mathbf{T}}^7$ modified duplex (**II**) has been performed during 500ps MD simulation employing modified version (parm98) of the AMBER [Cornell *et al*. (79)] force field. The duplex (**II**) has been solvated in TIP3P water (120-122) in a periodic box containing 5589 water molecules and 22 K^+ counter ions. Additional 25 KCl molecules corresponding to a 0.25M KCl concentration have been added to the respective systems to mimic the 0.1M NaCl ionic concentration used in the experiment. The atomic charges and the AMBER force field parameters of the $\underline{\mathbf{T}}$ oxetane modified nucleotide were obtained by *ab initio* calculation at the Hartree-Fock level employing the 6-31G* basis set, used to develop the X-PLOR force field parameters discussed above. The protocol is based on Cheatham-Kollman's (83) procedure and *Amber 6* program package (79) has been used. NMR constraints of 60 kcal mol^{-1}Å^{-2} for NOE, 40 kcal mol^{-1}rad^{-2} for dihedrals, 20 kcal mol^{-1}rad^{-2} for non integrated NOE constraints, have been used throughout the whole 0.5 ns MD simulation.

Computational Details of the MD Simulations

The protocol used in the 2.4 ns MD simulations (2 ns production runs) of the native and oxetane modified duplexes (Figure 1) is based on Cheatham-Kollman's (83) procedure employing a modified version (parm98) of the AMBER [Cornell *et al*. (79)] force field, as is implemented in *Amber 6* program package (123). The atomic charges and Amber force field parameters of the $\underline{\mathbf{T}}$ oxetane modified moiety were also imported from the *ab initio* calculation at the Hartree-Fock level employing the 6-31G* basis set, used to develop the X-PLOR force field param-

eters discussed above. The trajectories of the $\underline{\mathbf{T}}^7$ modified duplex (**II**) have been calculated starting from two different initial structures: (i) standard B-type DNA duplex (trajectory **D1**), built by 3DNA (124), and the NMR refined duplex (trajectory **D2**). TIP3P water (120-122) was used to introduce explicit solvent in the MD calculations. A periodic box containing 4413 and 5589 water molecules and 22 K^+ counter ions have been created around the **D1** and **D2** DNA duplexes, respectively. Additional 20 and 25 KCl molecules corresponding to a 0.25M KCl concentration have been added to the respective systems to mimic the 0.1M NaCl ionic concentration used in the experiment.

For the D2 trajectory the simulation protocol has been modified to make use of the NMR constraints during first 600 ps of the production run which had gradually been reduced from 60 kcal $mol^{-1}Å^{-2}$ for NOE, 40 kcal $mol^{-1}rad^{-2}$ for dihedrals, and 20 kcal $mol^{-1}rad^{-2}$ for non integrated NOE constraints to nothing in three steps: (i) to 30-20-10, respectively, after 100 ps; (ii) to 10-5-1 after 300 ps; and (iii) completely relaxed within 600 ps. These NMR constrained part of the simulation was followed by the 1.8 ns unconstrained-MD production run.

The solution dynamics of the native Dickerson-Drew dodecamer d(CGCGAATTCGCG)$_2$ (**I**) was modeled in an unconstrained 2.4 ns MD simulation (**N1** trajectory) employing same Cheatham-Kollman's (83) as for the oxetane modified **D1** and **D2** simulations above. TIP3P water (120-122) was used in a periodic box containing 4412 water molecules and 22 K Additional 20 and 25 KCl molecules corresponding to a 0.25M KCl concentration have been added to the respective systems to mimic the 0.1M NaCl ionic concentration used in the experiment.

The MD simulations of the native and oxetane modified DNA duplexes have been combined with the Molecular Mechanics Poisson-Boltzmann/surface area (MM-PBSA) (125, 126) calculations to analyze the total energy related to the DNA fragments. In this approach the gas phase energies for both DNA strands of the molecular structures obtained from the respective MD trajectories are calculated at the MM level without counter-ions and explicit water molecules and the solvation energies are estimated using a continuum approach (Poisson-Boltzmann/surface area) which utilizes the generalized Born model (127, 128) as it is implemented in MSMS (129) and GB auxiliary *Amber* programs for the calculations of non-polar and polar contributions to the solvation energy, respectively.

Stacking energies have been calculated using the model employed by Hobza *et al*. (96-99), taking the interactions inside and between the stacked bases into account, including the terms attributed to the hydrogen bonding, but neglecting all other interactions in the system. The sugar moieties of all residues were replaced by a hydrogen atom with a charge chosen to neutralize the molecule.

Acknowledgements

Generous financial support from the Swedish Natural Science Research Council (Vetenskapsrådet), the Swedish Strategic Research Foundation (Stiftelsen för Strategisk Forskning), European Union Biotechnology Program (LSHB-CT-2004-005276, Contract No. 005276), and Philip Morris USA, Inc. is gratefully acknowledged. The computational resources have been granted by the Swedish National Allocation Committee for the High Performance Computing and provided by the National Supercomputer Center (Linköping, Sweden) for what the authors are thankful for.

Supplemental Materials

Supplemental materials can be acquired, free of charge, from the contact author or from Adenine Press for $25.

Supplementary Material Available: Figure S1: The assignment of the H6/H8 to H1′ protons. Figure S2: Chemical shift correlation between the native duplex (**I**) and the $\underline{\mathbf{T}}^7$ modified duplex (**II**). Figure S3: The inter-residue NOEs used in the structure refinements. Figure S4: *R*- and *Q*-factors for the **D1** and **D2** trajectories. Figure S5: Total MM-PBSA energies (kcal/mol) and RMSd values (Å) along the MD trajectories. Figure S6: Stacking diagrams. Figure S7: Energy distributions (total MM-PBSA energy). Table SI: Chemical shifts of the $\underline{\mathbf{T}}^7$ modified dodecamer (**II**) compared to the native dodecamer (**I**). Table SII: The simulated DQF-COSY{^{31}P} coupling constants from NMRSIM. Table SIII: Simulated North:South populations using PSEUROT coupling constants in Table SII. Table SIV: γ^+ estimate using the approximation: $^{\%}\gamma^+ = 100\ (13.3 - J_{H4'5'} - J_{H4'5''})/9.7$. Table SV: Estimate of the epsilon torsion. Table SVI: Alfa and zeta estimates. Table SVII: Salt dependence of the melting of native and $\underline{\mathbf{T}}^7$ oxetane-modified duplexes. Table SVIII: Atomic charges of the oxetane modified thymidine phosphate (*ab initio*). Table SIX: Mean energy terms of the whole molecules. Table SX: Mean values of the energy terms for the individual residues. Table SXI: Mean energy differences (in kcal/mol) between the N1 trajectory and the D2 trajectory.

References and Footnotes

1. Kurreck, J., Wyszko, E., Gillen, C., and Erdmann, V. A. *Nucl. Acids Res. 30*, 1911-1918 (2002).
2. Yang, X., Han, X., Cross, C., Bare, S., Sanghvi, Y., and Gao, X. *Biochemistry 38*, 12586-12596 (1999).
3. Yang, X., Sanghvi, Y. S., and Gao, X. *J. Biomol. NMR 10*, 383-388 (1997).
4. Toulmé, J.-J. *Nature Biotech. 19*, 17-18 (2001).
5. Nguyen, D. H., DeFina, S. C., Fink, W. H., and Dieckmann, T. *J. Am. Chem. Soc. 124*, 15081-15084 (2002).
6. Dieckmann, T., Suzuki, E., Nakamura, G. K., and Feigon, J. *RNA 2*, 628-640 (1996).
7. Macaya, R. F., Schultze, P., Smith, F. W., Roe, J. A., and Feigon, J. *Proc. Natl. Acad. Sci. USA 90*, 3745-3749 (1993).
8. Baugh, C., Grate, D., and Wilson, C. *J. Mol. Biol. 301*, 117-128 (2000).
9. Sussman, D., Nix, J. C., and Wilson, C. *Nat. Struct. Biol. 7*, 53-57 (2000).
10. Amarzguioui, M. and Prydz, H. *Biochem. Biophys. Res. Comm. 316*, 1050-1058 (2004).
11. Elbashir, S. M., Harborth, J., Lendeckel, W., Yalcin, A., Weber, K., and Tuschl, T. *Nature 411*, 494-498 (2001).
12. Elbashir, S. M., Lendeckel, W., and Tuschl, T. *Genes. Dev. 15*, 188-200 (2001).
13. Ma, J.-B., Ye, K., and Patel, D. J. *Nature 429*, 318-322 (2004).
14. Tyagi, S. and Kramer, F. R. *Nature Biotechnol. 14*, 303-308 (1996).
15. Williams, J. C., Case-Green, S. C., Mir, K. U., and Southern, E. M. *Nucl. Acids Res. 22*, 1365-1367 (1994).
16. Cho, Y., Zhu, F. C., Luxon, B. A., and Gorenstein, D. G. *J. Biomol. Struct. Dyn. 11*, 685-702 (1993).
17. Mesmaeker, A. D., Altmann, K.-H., Waldner, A., and Wendeborn, S. *Curr. Op. Struct. Biol. 5*, 343-355 (1995).
18. Gonzalez, C., Stec, W., Reynolds, M. A., and James, T. L. *Biochemistry, 34*, 4969-4982 (1995).
19. Micklefield, J. *Curr. Med. Chem. 8*, 1157-1179 (2001).
20. Ikeda, H., Fernandez, R., Wilk, A., Barchi, J. J. J., Huang, X., and Marquez, V. E. *Nucl. Acids Res. 26*, 2237-2244 (1998).
21. Denisov, A. Y., Zamaratski, E. V., Maltseva, T. V., Sandström, A., Bekiroglu, S., Altmann, K.-H., Egli, M., and Chattopadhyaya, J. *J. Biomol. Struct. Dyn. 16*, 547-568 (1998).
22. Isaksson, J., Zamaratski, E., Maltseva, T. V., Agback, P., Kumar, A., and Chattopadhyaya, J. *J. Biomol. Struct. Dyn. 18*, 783-806 (2001).
23. Elhalabi, J. M. and Rice, K. G. *Curr. Med. Chem. 6*, 93-116 (1999).
24. Seela, F., Debelak, H., Rosemeyer, H., Thomas, H., Wenzel, T., and Zulauf, M. *Nucl. Acids Symp. Ser. 31*, 151-152 (1994).
25. Mitsui, T., Kitamura, A., Kimoto, M., To, T., Sato, A., Hirao, I., and Yokoyama, S. *J. Am. Chem. Soc. 125*, 5298-5307 (2003).
26. Kool, E. T. *Curr. Op. Chem. Biol. 4*, 602-608 (2000).
27. Gao, J., Watanabe, S., and Kool, E. T. *J. Am. Chem. Soc. 126*, 12748-12749 (2004).
28. Matsuda, S. and Romesberg, F. E. *J. Am. Chem. Soc. 126*, 14419-14427 (2004).
29. Henry, A. A., Olsen, A. G., Matsuda, S., Yu, C., Geierstanger, B. H., and Romesberg, F. E. *J. Am. Chem. Soc. 126*, 6923-6931 (2004).
30. Kim, T. W. and Kool, E. T. *Org. Letters 6*, 3949-3952 (2004).
31. Liu, H., Gao, J., and Kool, E. T. *J. Am. Chem. Soc. 127*, 1396-1402 (2005).
32. Lee, A. H. F. and Kool, E. T. *J. Org. Chem. 70*, 132-140 (2005).
33. Khaled, A., Ivannikova, T., and Auge, C. *Carbohyd. Res. 339*, 2641-2649 (2004).

34. Marquez, V. E., Siddiqui, M. A., Ezzitouni, A., Russ, P., Wang, J., Wagner, R. W., and Matteucci, M. D. *J. Med. Chem. 39*, 3739-3747 (1996).
35. Nielsen, K. E., Singh, S. K., Wengel, J., and Jacobsen, J. P. *Bioconjugate Chem. 11*, 228-238 (2000).
36. Bondensgaard, K., Petersen, M., Singh, S. K., Rajwanshi, V. K., Kumar, R., Wengel, J., and Jacobsen, J. P. *Chem. Eur. J. 6*, 2687-2695 (2000).
37. Sorensen, M. D., Kvaerno, L., Bryld, T., Håkansson, A. E., Verbeure, B., Gaubert, G., Herdewijn, P., and Wengel, J. *Nucl. Acids Res. Suppl. 1*, 25-26 (2001).
38. Sorensen, M. D., Kvaerno, L., Bryld, T., Håkansson, A. E., Verbeure, B., Gaubert, G., Herdewijn, P., and Wengel, J. *J. Am. Chem. Soc. 124*, 2164-2176 (2002).
39. Egli, M., Teplova, M., Minasov, G., Kumar, R., and Wengel, J. *Chem. Commun. 7*, 651-652 (2001).
40. Petersen, M., Bondensgaard, K., Wengel, J., and Jacobsen, J. P. *J. Am. Chem. Soc. 124*, 5974-5982 (2002).
41. Petersen, M., Håkansson, A. E., Wengel, J., and Jacobsen, J. P. *J. Am. Chem. Soc. 123*, 7431-7432 (2001).
42. Rajwanshi, V. K., Håkansson, A. E., Sorensen, M. D., Pitsch, S., Singh, S. K., Kumar, R., Nielsen, P., and Wengel, J. *Angew. Chem. Int. Ed. 39*, 1656-1659 (2000).
43. Singh, S. K., Nielsen, P., Koshkin, A. A., and Wengel, J. *Chem. Commun. 4*, 455-456 (1998).
44. Singh, S. K. and Wengel, J. *Chem. Commun. 12*, 1247-1248 (1998).
45. Vester, B. and Wengel, J. *Biochemistry 43*, 13233-13241 (2004).
46. Stein, H. and Hausen, P. *Science 166*, 393-395 (1969).
47. Hausen, P. and Stein, H. *Eur. J. Biochem. 14*, 278-283 (1970).
48. Pradeepkumar, P. I. and Chattopadhyaya, J. *J. Chem. Soc., Perkin. Trans. 2, 11*, 2074-2083 (2001).
49. Pradeepkumar, P. I., Zamaratski, E., Foldesi, A., and Chattopadhyaya, J. *Tetrahedron Lett. 41*, 8601-8607 (2000).
50. Pradeepkumar, P. I., Zamaratski, E., Földesi, A., and Chattopadhyaya, J. *J. Chem. Soc., Perkin. Trans. 2, 2*, 402-408 (2001).
51. Opalinska, J. B., Kalota, A., Gifford, L. K., Lu, P., Jen, K.-Y., Pradeepkumar, P. I., Barman, J., Kim, T. K., Swider, C. R., Chattopadhyaya, J. *et al. Nucleic Acids Research 32*, 5791 (2004).
52. Pradeepkumar, P. I. and Chattopadhyaya, J. *J. Chem. Soc., Perkin Trans. 2*, 2074 (2001).
53. Amirkhanov, N. V., Pradeepkumar, P. I., and Chattopadhyaya, J. *J. Chem. Soc., Perkin Trans. 2, 5*, 976 (2002).
54. Pradeepkumar, P. I., Amirkhanov, N. V., and Chattopadhyaya, J. *Org. Biomol. Chem. 1*, 81 (2003).
55. Boon, E. M., Barton, J. K., Pradeepkumar, P. I., Isaksson, J., Petit, C., and Chattopadhyaya, J. *Angew. Chem. Int. Ed. 41*, 3402-3405 (2002).
56. Summers, M. F., Byrd, R. A., Gallo, K. A., Samson, C. J., Zon, G., and Egan, W. *Nucl. Acids Res. 13*, 6375-6386 (1985).
57. Patel, D. J., Kozlowski, S., Marky, L. A., Broka, C., Rice, J. A., Itakura, K., and Breslauer, K. J. ***Journal??*** *21*, 428-436 (1982).
58. Feigon, J., Denny, W. A., Leupin, W., and Kearns, D. R. *Biochemistry 22*, 5930-5942 (1983).
59. Gronenborn, A. M. and Clore, G. M. *Prog. NMR Spect. 17*, 1-32 (1985).
60. Hare, D. R., Wemmer, D. E., Chou, S.-H., Drobny, G., and Reid, B. R. *J. Mol. Biol. 171*, 319-336 (1983).
61. Hosur, R. V., Govil, G., and Miles, H. T. *Magn. Reson. Chem. 26*, 927-944 (1988).
62. Scheek, R. M., Boelens, R., Russo, N., Van Boom, J. H., and Kaptein, R. *Biochemistry 23*, 1371-1376 (1984).
63. Van de Ven, F. J. M. and Hilbers, C. W. *Eur. J. Biochem. 178*, 1-38 (1988).
64. Varani, G., Aboul-ela, F., and Allain, F. H.-T. *Prog. NMR Spect. 29*, 51-127 (1996).
65. Kim, S.-G., Lin, L. J., and Reid, B. R. *Biochemistry, 31*, 3564-3574 (1992).
66. Dobson, C. M., Lian, L.-Y., Redfield, C., and Topping, K. D. *J. Magn. Reson. 69*, 201-209 (1986).
67. Maltseva, T. V., Yamakage, S. I., Agback, P., and Chattopadhyaya, J. *Nucl. Acids Res. 21*, 4288-4295 (1993).
68. De Leeuw, F. A. A. M. and Altona, C. *J. Comput. Chem. 4*, 428-437 (1983).
69. Pradeepkumar, P. I., Cheruku, P., Plashkevych, O., Acharya, P., Gohil, S., and Chattopadhyaya, J. *J. Am. Chem. Soc. 126*, 11484-11499 (2004).
70. Chary, K. V. R., Rastogi, V. K., and Govil, G. *J. Magn. Reson. Series B*, 102, 81-83 (1993).
71. Chou, S.-H., Zhu, L., Gao, Z., Cheng, J. W., and Reid, B. R. *J. Mol. Biol. 264*, 981-1001 (1996).
72. Gorenstein, D. G. *Chem. Rev. 94*, 1315-1338 (1994).
73. Rinkel, L. J. and Altona, C. *J. Biomol. Struct. Dyn. 4*, 621-649 (1987).
74. Roongta, V. A., Jones, C. R., and Gorenstein, D. G. *Biochemistry 29*, 5245-5258 (1990).
75. Brünger, A. T. 3.1 Ed. Yale University Press, New Haven, CT (1990)..
76. A. D. MacKerell, J., Bashford, D., Bellott, M, Jr., R. L. D., Evanseck, J. D., Field, M. J., Fischer, S., Gao, J., Guo, H., Ha, S. *et al. J. Phys. Chem. B 102*, 3586-3616 (1998).
77. Borgias, B. A. and James, T. L. *J. Magn. Reson. 87*, 475-487 (1990).
78. Borgias, B. A., Thomas, P. D., Liu, H., Kumar, A., and James, T. L. University of California, San Fransisco, CA. (1993).

79. Cornell, W. D., Cieplak, P., Bayly, C. I., Gould, I. R., Merz, K. M. J., Ferguson, D. M., Spellmeyer, D. C., Fox, T., Caldwell, J. W., and Kollman, P. A. *J. Am. Chem. Soc. 117*, 5179-5197 (1995).
80. Feig, M. and Pettitt, B. M. *Biophysical Journal 75*, 134-149 (1998).
81. Feig, M. and Pettitt, B. M. *J. Phys. Chem. B 101*, 7361-7363 (1997).
82. Beveridge, D. L., Swaminathan, S., Ravishanker, G., Withka, J. M., Srinivasan, J., Prevost, C., Louise-May, S., Langley, D. R., DiCapua, F. M., and Bolton, P. H. *Molecular Dynamics Simulations on the Hydration, Structure, and Motions of DNA Oligomers*. Macmillan Press, Riverside, NJ (1993).
83. Cheatham, T. E., III and Kollman, P. A. *J. Am. Chem. Soc. 119*, 4805-4825 (1997).
84. Cheatham, T. E., III and Young, M. A. *Biopolymers 56*, 232-256 (2001).
85. Hirshberg, M. and Levitt, M. *Dynamics and Problem of Recognition in Biological Macromolecules*. Plenum Press, New York (1996).
86. Jayaram, B., MacConnell, K., Dixit, S. B., Surjit, B., and Beveridge, D. L. *J. Comp. Phys. 151*, 333-357 (1999).
87. Jayaram, B., Sprous, D., Young, M. A., and Beveridge, D. L. *J. Am. Chem. Soc. 120*, 10629-10633 (1998).
88. Kollman, P. A., Massova, I., Reyes, C., Kuhn, B., Huo, S., Chong, L., Lee, M., Lee, T., Duan, Y., Wang, W. *et al. Acc. Chem. Res. 33*, 889-897 (2000).
89. McConnell, K. J. and Beveridge, D. L. *J. Mol. Biol. 304*, 803-820 (2000).
90. Wang, L., Hingerty, B. E., Srinivasan, A. R., Olson, W. K., and Broyde, S. *Biophys. J. 83*, 382-406 (2002).
91. Yan, S. and Shapiro, R. *J. Am. Chem. Soc. 123*, 7054-7066 (2001).
92. Young, M. A., Ravishanker, G., and Beveridge, D. L. *Biophys. J. 73*, 2313-2336 (1997).
93. Wu, Z., Delaglio, F., Tjandra, N., Zhurkin, V. B., and Bax, A. *J. Biomol. NMR 26*, 297-315 (2003).
94. Kool, E. T. *Annu. Rev. Biophys. Biomol. Struct. 30*, 1-22 (2001).
95. Senger, W. *Principles of Nucleic Acid Structure*. Springer Verlag, Berlin (1988).
96. Sponer, J., Gabb, H. A., Leszczynski, J., and Hobza, P. *Biophys. J. 73*, 76-87 (1997).
97. Sponer, J., Leszczynski, J., and Hobza, P. *J. Phys. Chem. 100*, 1965-1974 (1996).
98. Sponer, J., Leszczynski, J., and Hobza, P. *J. Mol. Struct. 573*, 43-53 (2001).
99. Sponer, J., Leszczynski, J., and Hobza, P. *Biopolymers 61*, 3-31 (2002).
100. Bhattacharya, P. K. and Barton, J. K. *J. Am. Chem. Soc. 123*, 8649-8656 (2001).
101. Bhattacharya, P. K., Cha, J., and Barton, J. K. *Nucl. Acids Res. 30*, 4740-4750 (2002).
102. Denisov, V. P., Carlström, G., Venu, K., and Halle, B. *J. Mol. Biol. 268*, 118-136 (1997).
103. Maltseva, T., Zarytova, V. F., and Chattopadhyaya, J. *J. Biochem. Biophys. Meth 30*, 163-177 (1995).
104. Maltseva, T. V., Altmann, K.-H., Egli, M., and Chattopadhyaya, J. *J. Biomol. Struct. Dyn. 16*, 569-578 (1998).
105. Maltseva, T. V., and Chattopadhyaya, J. *Tetrahedron 51*, 5501-5508 (1995).
106. Otting, G., Liepinsh, E., and Wüthrich, K. *Science 254*, 974-980 (1991).
107. Shan, S.-o. and Herschlag, D. *Biochemistry 93*, 14474-14479 (1996).
108. Shan, S.-o., Loh, S., and Herschlag, D. *Science 272*, 97-101 (1996).
109. Otting, G., Liepinsh, E., Farmer, B. T. I., and Wüthrich, K. *J. Biomol. NMR 1*, 209-215 (1991).
110. Leijon, M. and Gräslund, A. *Nucl. Acids Res. 20*, 5339-5343 (1992).
111. Guéron, M., Kochoyan, M., and Leroy, J. L. *Nature 328*, 89-92 (1987).
112. Leroy, J. L., Kochoyan, M., Huynh-Dinh, T., and Guéron, M. *J. Mol. Biol. 200*, 223-238 (1988).
113. Pardi, A., Morden, K. M., Patel, D. J., and Tinoco, I. *Biochemistry 21*, 6567-6574 (1982).
114. Pardi, A., Morden, K. M., Patel, D. J., and Tinoco, I. *Biochemistry 22*, 1107-1113 (1983).
115. Pardi, A. and Tinoco, I. *Biochemistry 21*, 4686-4693 (1982).
116. Wärmländer, S., Sponer, J. E., Sponer, J., and Leijon, M. *J. Biol. Chem. 277*, 28491-28497 (2002).
117. Hrebabecky, H. and Farkas, J. *Collect. Czech. Chem. Commun., 39*, 1098 (1974).
118. Bruker Analytik GmbH. (1991).
119. Omichinski, J. G., Pedone, P. V., Felsenfeld, G., Gronenbron, A. M., and Clore, G. M. *Nature Struct. Biol. 4*, 122-132 (1997).
120. Jorgensen, W. L. *J. Am. Chem. Soc. 103*, 335-340 (1981).
121. Jorgensen, W. L. *J. Am. Chem. Soc. 103*, 341-345 (1981).
122. Jorgensen, W. L., Chandrasekhar, J., Madura, J. D., Impey, R. W., and Klein, M. L. *J. Chem. Phys. 79*, 926-935 (1983).
123. Case, D. A., Pearlman, D. A., Caldwell, J. W., Cheatham, T. E., III, Ross, W. S., Simmerling, C. L., Darden, T. A., Merz, K. M. J., Stanton, R. V., Cheng, A. L. *et al*. University of California, San Francisco (1999).
124. Lu, X.-J. and Olson, W. K. *Nucl. Acids Res. 31*, 5108-5121 (2003).
125. Srinivasan, J., Miller, J., Kollman, P. A., and Case, D. A. *J. Biomol. Struct. Dyn. 16*, 671-682 (1998).
126. Wang, J., Morin, P., Wang, W., and Kollman, P. A. *J. Am. Chem. Soc. 123*, 5221-5230 (2001).
127. Tsui, V. and Case, D. A. *J. Am. Chem. Soc. 122*, 2489-2498 (2000).
128. Tsui, V. and Case, D. A. *Biopolymers 56*, 275-291 (2001).
129. Sanner, M. F., Olson, A. J., and Sphener, J. C. *Biopolymers 38*, 305-320 (1996).

Date Received: June 10, 2005

Communicated by the Editor Ramaswamy H Sarma